SECOND-ORDER ACCURATE METHOD FOR SOLVING

RADIATION-HYDRODYNAMICS

A Dissertation

by

JARROD DOUGLAS EDWARDS

Submitted to the Office of Graduate and Professional Studies of
Texas A&M University
in partial fulfillment of the requirements for the degree of

DOCTOR OF PHILOSOPHY

Chair of Committee,   Jim Morel
Co-Chair of Committee, Marvin Adams
Committee Members,   Jean Ragusa
                         Jean-Luc Guermond
Head of Department,   Yassin Hassan

December 2013

Major Subject: Nuclear Engineering

ABSTRACT

Second-order discretizations for radiation-hydrodynamics is currently an area of great interest. Second-order methods used to solve the respective single-physics problems often differ fundamentally, making it difficult to combine them in a second-order manner. Here, we present a method for solving the equations of radiation hydrodynamics that is second-order accurate in space and time. We achieve this accuracy by combining modern methods used in standard single-physics calculations.

This method is defined for a 1-D model of compressible fluid dynamics coupled with grey radiation diffusion and combines the MUSCL-Hancock method for solving the Euler equations with the TR/BDF2 scheme in time and a linear-discontinuous finite-element method in space for solving the equations of radiative transfer. Though uncommon for radiation diffusion calculations, the linear-discontinuous method is a standard for radiation transport applications. We address the challenges inherent to using different spatial discretizations for the hydrodynamics and radiation components and demonstrate how these may be overcome. Using the method of manufactured solutions, we show that the method is second-order accurate in space and time for both the equilibrium diffusion and streaming limit, and we show that the method is capable of computing radiative shock solutions accurately by comparing our results with semi-analytic solutions.

DEDICATION

This work is dedicated to my father and mother, Harold and Terry Edwards, and to my aunt, Judith Nash, for their unwavering support, encouragement, and love.

ACKNOWLEDGEMENTS

First, I would like to acknowledge my adviser, Dr. Jim Morel. Both in the classroom and through countless hours of one on one instruction, he has patiently guided me through this research process and has taught me so much about radiation transport and radiation hydrodynamics. Furthermore, through his example and by pushing me to be better, he has shown me what rigor, professionalism, and excellence in conducting research looks like.

Next, I would like to acknowledge Dr. Rob Lowrie, my mentor over the course of two summer internships at Los Alamos National Laboratory and a research colleague throughout my doctoral research. Rob introduced me to hydrodynamics, shocks, and asymptotics and has generously included me in very exciting research opportunities that expanded my knowledge of the field. Over the years, his advice has been invaluable to me in my rad-hydro research.

I would also like to acknowledge my co-adviser Dr. Marvin Adams and my committee members Dr. Jean Ragusa and Dr. Jean-Luc Guermond. I have learned a lot from each of these men both through coursework and through our personal interactions as I've pursued this research. Their insights and suggestions made this work more thorough and complete. Of course, I'm also very grateful to Marv for bringing me to Texas A&M in the first place and for giving me an opportunity to work with him and our research group.

Many co-workers, classmates, and officemates have helped me through this process. These include, but are not limited to, Dr. Teresa Bailey, Dr. Alex Maslowski,

Andrew Till, Akansha Kumar, Dr. Jim Ferguson, Dr. Adam Hetzler, and Carolyn McGraw. I would especially like to acknowledge Don Bruss, whose support, positive outlook, and encouraging spirit have been an inspiration to me. One of the benefits to working in a small research community is the hope that I will continue to get to work with these folks throughout my career, and it is a privilege to consider each of them colleagues and friends.

Even more so, I could not have completed this work without my family and the close friends who have become like family to me. Their unwavering support and encouragement have kept me going throughout this process, and their love has given it meaning.

Most of all, I'd like to acknowledge my God and my Savior, Jesus Christ. Though being God, himself, Jesus became a man, lived a sinless life, and died to pay the price of my sin in God's sight and to purchase my forgiveness. Through faith alone in him, my relationship with God has been eternally restored. That relationship is the source of my strength, hope, and peace every day, and his glory and pleasure are the inspiration and goal of this work.

NOMENCLATURE

RH	Radiation-Hydrodynamics
LDFEM	Linearly Discontinuous Finite Element Method
MHM	MUSCL Hancock Method
IMEX	Implicit/Explicit
ISP	Isothermal Sonic Point
CN	Crank-Nicholson

TABLE OF CONTENTS

LIST OF FIGURES

ix

LIST OF TABLES

1. INTRODUCTION

Radiation hydrodynamics (RH) describes thermal radiation propagating through a fluid and the effects of the radiation on the properties of that fluid. Second-order time integration in problems involving radiation hydrodynamics is currently an area of great interest. Though detailed work has been done for time integration of radiation diffusion and transport [21, 16, 11, 25, 1, 30, 4], and likewise for fluid dynamics [31], research in second-order methods that couple the two has only recently been approached [19, 3, 5]. Because of the dramatically different time scales of radiation diffusion/transport and fluid advection, RH calculations are usually treated using an implicit/explicit (IMEX) scheme [19, 3, 5]. In such algorithms, the fluid advection component, which changes at a much slower rate, is treated explicitly; whereas, the radiation diffusion and energy exchange terms are treated implicitly.

Sekora and Stone developed a scheme for RH that uses second-order Godunov methods to achieve second-order accuracy in space and time. This scheme is entirely explicit so that the time step is limited by the more rapidly varying radiation time scale [28]. Sekora's method is intended for the relativistic regime characterized as $c/a_\infty < 10$. In this case, the material and radiation time-scales aren't dramatically different, and therefore, the Courant limit time-step constraint isn't overly restrictive. However, for the non-relativistic regime, i.e. $c/a_\infty >> 1$, bounding the time-step according to the radiation time-scale will force the time steps to be orders of magnitude smaller than the material time-scale. Kadioglu has also developed a second-order accurate scheme for both low and high energy density RH problems [10, 9]. Accuracy is achieved by incorporating the explicit algorithm into the implicit iterations. While this provides a tight coupling between the explicit and implicit terms, it is compu-

tationally more expensive than standard IMEX schemes, since the explicit block is solved in each nonlinear iteration [10].

In this work, we derive, implement, and test a new IMEX scheme for solving the equations of radiation hydrodynamics that is second-order accurate in space and time. We consider a RH system that combines a 1-D slab model of compressible fluid dynamics with a grey radiation diffusion model. Specifically, we use the MUSCL-Hancock Method (MHM) to solve the fluid advection component explicitly in space and time and the TR/BDF2 scheme to solve the radiation diffusion component and energy exchange terms implicitly in time. We discretize our diffusion scheme in space using a linearly-discontinuous finite element method (LDFEM). We discretize the diffusion scheme in such a way that, if we were to extend our method to P_1, it would be equivalent to an S_2 LDFEM spatial discretization for radiation transport. This is not a common scheme for discretizing the diffusion equation, but as explained later, it enables us to address a critical issue associated with radiation transport even though we use a diffusion approximation. We base our radiation-hydrodynamics method upon existing hydrodynamics and radiation diffusion algorithms, and it reduces to those respective algorithms when the effects of the coupled physics are negligible.

The class of MUSCL schemes is an example of second-order methods for solving fluid advection problems. One such widely used scheme is the MHM. [31] This is a four step process, each of which is explicit, that is second-order accurate in both space and time. The first step involves reconstructing an independent linear representation within each spatial cell from the initial cell-centered data. The cell averages are evolved by a half-step in time while keeping the slopes fixed. The resulting linearized data is then used with a Riemann solver to compute second-order accurate flux values on the cell edges at the half-time step. Finally, using these flux values, the cell-centered data is evolved over a full time step.

One of the most common methods for solving the radiation diffusion equation in time is the Crank-Nicholson method, also known as the Trapezoid Rule. This is a well-known, implicit method that is second-order accurate; however, its principal drawback is that it can become highly oscillatory for stiff systems. An alternative to this is a linearly discontinuous Galerkin method in time. Despite the fact that this scheme is more accurate than the Crank-Nicholson method and damps oscillations quickly, it is much more costly computationally being roughly equivalent to solving two Crank-Nicholson systems simultaneously over each time step. [32] In this work, we use the TR/BDF2 scheme for discretizing the radiation diffusion and energy exchange terms in time. The TR/BDF2 scheme is a one-step, two-stage implicit method that was first derived in [2]. [1] There is actually a family of such schemes, but one member of the family can be shown to be optimal in a certain sense. In Section 3, we compare in detail a simple, near-optimal version of the TR/BDF2 method with the Crank-Nicholson method applied to the radiative transfer equations. This near-optimal TR/BDF2 scheme consists of a Crank-Nicholson step over half the time step and, using that solution, a BDF2 solve over the remainder the time step. We also compare various treatments of the non-linearities in the radiative transfer equations using this near-optimal TR/BDF2 scheme. The results of this study were published in [7].

A critical issue for radiation transport spatial discretizations is the preservation of the diffusion limit. Due to limitations on computational resources, it is often necessary for regions of a given mesh to be optically thick, i.e. for a given cell to encompass many mean-free-paths. In many cases, these cells are dominated by non-terminal collision processes like scattering or, in the case of radiative transfer, absorption and

---

[1]Here we use the term "stage" to refer to an implicit equation that must be solved within each time step in a discretization scheme, but as explained in Section 2.3.4, the same term can have a slightly different meaning when referring to Runge-Kutta methods.

re-emission. In these cases, diffusion theory represents a good approximation to the transport process. However, not all transport spatial discretizations are guaranteed to reproduce the correct diffusion solution in a diffusive region without requiring a spatial resolution that is exceedingly costly. [14] Likewise, even though we use a radiation diffusion model for our radiation-hydrodynamics system, because we discretize our diffusion equation in first-order form, it is possible that the discrete equations will fail to have the diffusion limit in highly diffusive problems. So, for this work, we use an LDFEM discretization, common in radiation transport calculations, for the diffusion equation because it enables us to investigate the diffusion limit for transport discretizations without the complications of a full transport treatment.

The MHM includes spatial differencing for the advection equations and incorporates a linear interpolation from cell-averaged values to compute the slopes. However, Lowrie and Morel show in [18] that interpolation schemes which only depend on the mesh geometry and do not incorporate additional physical data, e.g. cross-section values, fail to have the diffusion limit. Furthermore, the differences in spatial discretization between the advection and diffusion equations present considerable complications due to the fact that, in the MHM, the slopes are determined from interpolations of the cell-centered unknowns; whereas, in the LDFEM, the slopes are computed as part of the solution to the discretized spatial moment equations. To add to these complications, the internal energy of the material represents an unknown in both the material advection and radiation diffusion equations. The easy solution to this problem is to recompute the internal energy and radiation slopes at the beginning of each time step using the MHM limiter. Doing this, we were able to show that our method maintained the diffusion limit in 1D and reproduced shock solutions accurately. However, standard 2D and 3D hydrodynamics limiters use a spatial representation that will not maintain the diffusion limit. Thus, to overcome

4

this limitation, the method we present here preserves the slopes computed by the LDFEM from one time step to the next. We use reconstructed slopes as determined in the MUSCL-Hancock method only to compute the advection fluxes, and we use the preserved LDFEM slopes to initialize the implicit calculations for the radiation energy density and flux and for the material temperature update. This allows our method to reduce to its standard constituent methods when the contributions from coupled physics are negligible, and we believe it will also allow us to preserve the diffusion limit in the future extension of our method to 2D and 3D.

The scheme consists of two main cycles. In the first cycle, we use the MHM to compute the fluid advection explicitly over half the time step, and we use the Crank-Nicholson scheme to update the terms affected by the radiation implicitly. In the second cycle, we use the MHM, again, to compute the fluid advection component over the remainder of the time step and the BDF2 scheme to compute the implicit radiation component. One advantage to applying the full MHM over each half time step is that, if the time step size is being determined by the Courant limit, we can take twice the usual time step. In this case, the cost of two diffusion solves per time step is mitigated. Furthermore, the scheme is designed in such a way that, if the radiation contributions to the hydrodynamics are negligible, the standard MHM solution is obtained over each half time step, and if the hydrodynamics contributions to the radiation diffusion are negligible, the standard TR/BDF2 solution for radiative transfer is over the full time step.

The remainder of this thesis is structured as follows. We begin in Section 2 by describing the algorithms and properties of MUSCL-Hancock, TR/BDF2, and LDFEMs in greater detail. Then, in Section 3, we investigate the performance of the TR/BDF2 scheme applied to the equations of radiative transfer using a variety of treatments for the non-linearities and compare the results with Crank-Nicholson. In

Section 4, we describe our second-order accurate radiation-hydrodynamics method in detail, and in Sections 5 and 6, we demonstrate the performance of this method. In Section 5, we use the method of manufactured solutions to show that our method is second-order accurate in both space and time for the equilibrium diffusion limit as well as the streaming limit. Then, in Section 6, we demonstrate the capability of our method to accurately compute radiation-hydrodynamic shocks by reproducing semi-analytic shock solutions. Finally, in Section 7, we summarize our results, and in Section8, we present our conclusions and recommendations for future work.

2. CONSTITUENT METHODS

In this section, we discuss the consituent methods of our rad-hydro scheme. Specifically, we describe, in detail, the MUSCL-Hancock Method, the TR/BDF2 scheme, and the LDFEM spatial discretization of our radiation equations. Each of these methods represents an integral component to our overall IMEX rad-hydro scheme.

The physical system we model couples the 1-D equations of compressible fluid dynamics with a grey radiation diffusion model. This rad-hydro system may be written as:

$$\frac{\partial \rho}{\partial t} + \frac{\partial}{\partial x}\left(\rho u\right) = 0 \,, \tag{2.1a}$$

$$\frac{\partial}{\partial t}\left(\rho u\right) + \frac{\partial}{\partial x}\left(\rho u^2\right) + \frac{\partial}{\partial x}\left(p\right) = \frac{\sigma_t}{c}F_{r,0} \,, \tag{2.1b}$$

$$\frac{\partial E}{\partial t} + \frac{\partial}{\partial x}\left[\left(E + p\right)u\right] = -\sigma_a c\left(aT^4 - E_r\right) - \frac{\sigma_t u}{c}F_{r,0} \,, \tag{2.1c}$$

$$\frac{\partial E_r}{\partial t} + \frac{\partial F_r}{\partial x} = \sigma_a c\left(aT^4 - E_r\right) + \frac{\sigma_t u}{c}F_{r,0} \,, \tag{2.1d}$$

$$\frac{c}{3}\frac{\partial E_r}{\partial x} = -\frac{\sigma_t}{c}F_{r,0} \,, \tag{2.1e}$$

where ρ is the density, u is the velocity, E is the total material energy, E_r is the radiation energy density, F_r is the radiation flux, and $F_{r,0}$ is given by:

$$F_{r,0} = F_r - \frac{4}{3}\frac{u}{c}E_r \,. \tag{2.2}$$

Note that, while we write the radiation equations in P_1 form, there is no time derivative in Eq. (2.1e); so, Eqs. (2.1d) and (2.1e) fundamentally represent a diffusion

equation. By writing the radiation diffusion equation in this manner, the treatment of the momentum deposition and radiation advection terms is more straight-forward, as is the extension of the method to radiation transport.

Furthermore, we use a simplified model for material motion treatment developed by Morel which analytically preserves the equilibrium diffusion limit through first-order v/c [24]. This approximation also yields correct equilbrium values for energy-integrated quantities and is conservative in momentum and energy; though, our scheme will not conserve momentum, since we don't have a radiation momentum conservation statement.

Mathematically, Eq. (2.1) typically does not have a unique weak solution in and of itself. In order to establish uniqueness, we identify the following condition for the desired physical solution in the presence of a discontinuity:

$$a_L^* > S > a_R^*, \tag{2.3}$$

where a_L^* and a_R^* are the radiation-modified speeds of sound of the material just to the left and right, respectively, of a given solution discontinuity, which is moving at speed S. As explained in [15], this condition implies that the solution propagating along characteristic lines in the x/t plane intersect the discontinuity as t increases, and conversely, that no characteristic traced in the direction of decreasing t will intersect a line of discontinuity. Thus, every solution point in the x/t plane can be connected via characteristic lines to a point in the initial condition. Because the intersection of characteristics at a discontinuity results in an increase in entropy for compressible fluid flow, Eq. (2.3) is referred to as the entropy condition, or Lax inequality.

Separating the more slowly-varying fluid advection terms from the radiation diffusion and exchange terms, and ignoring radiation momentum deposition terms for

the time being, the pure hydrodynamic component is given by:

$$\frac{\partial \rho}{\partial t} + \frac{\partial}{\partial x} \left(\rho u \right) = 0 \, , \tag{2.4a}$$

$$\frac{\partial}{\partial t} \left(\rho u \right) + \frac{\partial}{\partial x} \left(\rho u^2 \right) + \frac{\partial p}{\partial x} = 0 \, , \tag{2.4b}$$

$$\frac{\partial E}{\partial t} + \frac{\partial}{\partial x} \left[\left(E + p \right) u \right] = 0 \, . \tag{2.4c}$$

The more rapidly-varying equations involving radiation diffusion and material energy exchange, then, are given by:

$$\frac{\partial E}{\partial t} = -\sigma_a c \left(a T^4 - E_r \right) - \sigma_t \frac{u}{c} \left(\frac{4}{3} E_r u - F_r \right) \, , \tag{2.5a}$$

$$\frac{\partial E_r}{\partial t} + \frac{\partial F_r}{\partial x} = \sigma_a c \left(a T^4 - E_r \right) + \sigma_t \frac{u}{c} \left(\frac{4}{3} E_r u - F_r \right) \, , \tag{2.5b}$$

$$\frac{1}{3} \frac{\partial E_r}{\partial x} + \frac{\sigma_t}{c} F_r = \sigma_t \frac{4}{3} E_r \frac{u}{c} \, . \tag{2.5c}$$

Additionally, throughout this thesis, we use the cm-jerk-shake unit system in which 1 jerk = 10^9 Joules and 1 shake = 10^{-8} seconds. Furthermore, the spatial domain is a 1-D mesh where cell "i" is defined as $x = \left\{ x : x \in \left(x_{i-1/2}, x_{i+1/2} \right) \right\}$, and

$$\Delta x_i = x_{i+1/2} - x_{i-1/2} \, . \tag{2.6}$$

2.1   MUSCL-Hancock Method

The MUSCL-Hancock method is a widely used scheme for solving the hydrodynamic conservation equations, given by Eqs. (2.4). Writing Eqs. (2.4) in operator form, we have:

$$\frac{\partial U}{\partial t} + \frac{\partial F \left(U \right)}{\partial x} = 0 \, , \tag{2.7}$$

where

$$F = \begin{bmatrix} \rho u \\ \rho u^2 + p \\ (E + p)\, u \end{bmatrix}. \tag{2.8}$$

The first step in the MUSCL-Hancock Method is to perform a reconstruction step, linearizing the cell-averaged data, U_i^n:

$$U_{L,i}^n = U_i^n - \frac{\Delta_i^n}{2}; \quad U_{R,i}^n = U_i^n + \frac{\Delta_i^n}{2}, \tag{2.9}$$

where

$$U_i = \begin{bmatrix} \rho_i \\ (\rho u)_i \\ E_i \end{bmatrix}, \tag{2.10}$$

and Δ_i^n is the slope in cell i determined from the cell-centered data. The simplest form of Δ_i is:

$$\Delta_i^n = \frac{1 - \omega}{2} \left(U_i^n - U_{i-1}^n \right) + \frac{1 + \omega}{2} \left(U_{i+1}^n - U_i^n \right), \tag{2.11}$$

where ω is chosen based on how much relative weight the user wants to give to the left or right differences. To solve the problems in this thesis, we use $\omega = 0$. The slope obtained in Eq. (2.11) may also be modified using some type of slope or flux limiter to reduce spurious oscillations, which may be produced near strong gradients. Some examples of these limiters include minmod, superbee, and vanLeer, which are described in [31]. We note that no proof exists that these limiters converge to the entropy solution, i.e. the desired physical solution, for Eqs. (2.4). In fact, for a generalized minmod limiter, given by:

$$\Delta_i^n = minmod\left(\theta\frac{U_i^n - U_{i-1}^n}{\Delta x}, \frac{U_{i+1}^n - U_{i-1}^n}{2\Delta x}, \theta\frac{U_{i+1}^n - U_i^n}{\Delta x}\right),\qquad(2.12)$$

with $\theta > 1$, Kurganov et al show that, for a 1D scalar conservation law, in some cases the limited solution does not converge to the entropy solution [12]. However, for the dissipative limit, i.e. the "standard" minmod limiter where $\theta = 1$, their results show that it does converge to the entropy solution for all tested cases. For our radiative shock tests in Section 6, we use the standard minmod limiter, and we see that our results do converge to the correct semi-analytic solutions.

After the data is reconstructed, the hydrodynamic cell-averages are evolved over a half time step:

$$U_i^{n+1/2} = U_i^n + \frac{\Delta t^n}{2\Delta x_i}\left(F_{L,i}^n - F_{R,i}^n\right).\qquad(2.13)$$

where

$$F_{L,i}^n = F\left(U_{L,i}^n\right), F_{R,i}^n = F\left(U_{R,i}^n\right).\qquad(2.14)$$

The half-step values are then used in conjunction with a Riemann solver to compute the cell-edge fluxes at $t^{n+1/2}$, $F_{i+1/2}^{n+1/2}$. The Riemann problem and various Riemann solvers are described in detail in [31]. One such Riemann solver is the HLL Riemann solver, which assumes that the exact solution space consists of three regions separated by the two fastest signal velocities, i.e. a two-wave model. In this research, we use the HLLC approximate Riemann solver to compute the intercell fluxes. The HLLC Riemann solver modifies the HLL solver by incorporating a third wave, which accurately restores the contact wave from the Euler equations. Once we've computed the fluxes, we use them to determine the final MUSCL-Hancock solution, U_i^{n+1}:

$$U_i^{n+1} = U_i^n + \frac{\Delta t}{\Delta x}\left(F_{i-1/2}^{n+1/2} - F_{i+1/2}^{n+1/2}\right). \tag{2.15}$$

2.2 Linearly Discontinuous Finite Element Method in Space

In discretizing the radiative transfer equations in space, we want to preserve second-order accuracy for the radiation energy density, radiation energy flux, and material temperature. To do this, we apply a linear-discontinuous Galerkin approximation to Eq. (2.5). In this section, we neglect material motion terms for simplicity, and we rewrite Eq. (2.5a) in terms of material temperature to make treating the non-linearities in the Planck source term more straightforward. We also neglect including the kinetic energy terms, since they can be treated as an external source in the implicit calculation. Thus, the remaining material temperature equation is given by:

$$C_v \frac{\partial T}{\partial t} = \sigma_a c\left(E - aT^4\right) + Q. \tag{2.16}$$

We approximate the solution in each cell using a linear representation. To accomplish this, we define a set of tent functions as our basis, each of which has a value of 1 at a given vertex and 0 at all the other vertices. So, for a given cell, the two non-zero basis functions in that cell may be defined as:

$$b_L\left(x\right) = \frac{x_{i+1/2} - x}{x_{i+1/2} - x_{i-1/2}}, \tag{2.17a}$$

$$b_R\left(x\right) = \frac{x - x_{i-1/2}}{x_{i+1/2} - x_{i-1/2}}. \tag{2.17b}$$

Using these basis functions, we define the radiation energy density, radiation energy

flux, and material temperature inside a given cell i as:

$$E_r(x) = E_{r,L}b_L + E_{r,R}b_R\,, \tag{2.18a}$$

$$F_r(x) = F_{r,L}b_L + F_{r,R}b_R\,, \tag{2.18b}$$

$$T(x) = T_L b_L + T_R b_R\,. \tag{2.18c}$$

Furthermore, we allow the solution to be discontinuous at cell interfaces so that, for example, $E_{r,R,i-1}$ may not necessarily be equal to $E_{r,L,i}$. This overall approach is called a linearly discontinuous Galerkin method and is very similar to the method described by Reed and Hill to discretize the steady-state S_2 neutron transport equation [26].

We obtain the weak form of the solution to the balance equation by multiplying (2.5b) by a generic test function and integrating over the width of the cell, yielding:

$$\int_{x_{i-1/2}}^{x_{i+1/2}} b_k \frac{\partial E_r}{\partial t}\, dx + \int_{x_{i-1/2}}^{x_{i+1/2}} b_k \frac{\partial F_r}{\partial x}\, dx = \int_{x_{i-1/2}}^{x_{i+1/2}} b_k \sigma_a c\left(aT^4 - E_r\right)\, dx\,. \tag{2.19}$$

Then, using integration by parts, we have:

$$\int_{x_{i-1/2}}^{x_{i+1/2}} b_k \frac{\partial E_r}{\partial t}\, dx + \left[(b_k F_r)\,|_{x=x_{i+1/2}} - (b_k F_r)\,|_{x=x_{i-1/2}} - \int_{x_{i-1/2}}^{x_{i+1/2}} F_r \frac{\partial b_k}{\partial x}\, dx \right]$$
$$= \int_{x_{i-1/2}}^{x_{i+1/2}} b_k \sigma_a c\left(aT^4 - E_r\right)\, dx\,. \tag{2.20}$$

Using a similar process with (2.5c), we derive the weak form of the solution for the radiation energy flux:

13

$$\frac{c}{3}\left[\left(b_k E_r\right)|_{x=x_{i+1/2}} - \left(b_k E_r\right)|_{x=x_{i-1/2}} - \int_{x_{i-1/2}}^{x_{i+1/2}} E_r \frac{\partial b_k}{\partial x}\, dx\right]$$

$$+ \int_{x_{i-1/2}}^{x_{i+1/2}} b_k \sigma_t F_r\, dx = 0\,. \tag{2.21}$$

At this point we need expressions relating $E_{r,i-1/2}$ and $F_{r,i-1/2}$, the edge values of E_r and F_r, respectively, to interior values. These relationships are obtained via the characteristic variables:

$$\epsilon^+ = \frac{c}{2}E_r + \frac{\sqrt{3}}{2}F_r\,, \tag{2.22a}$$

and

$$\epsilon^- = \frac{c}{2}E_r - \frac{\sqrt{3}}{2}F_r\,. \tag{2.22b}$$

The first characteristic variable, ϵ^+ represents an angular radiation intensity that propagates from left to right, while the second characteristic variable, ϵ^- represents an angular radiation intensity that propagates from right to left. These characteristic variables are defined at the cell edges via upwinding:

$$\epsilon_{i-1/2}^+ = \frac{c}{2}E_{r,R,i-1} + \frac{\sqrt{3}}{2}F_{r,R,i-1}\,, \tag{2.23a}$$

$$\epsilon_{i-1/2}^- = \frac{c}{2}E_{r,L,i} - \frac{\sqrt{3}}{2}F_{r,L,i}\,. \tag{2.23b}$$

Using the above definitions, we can determine the edge values $E_{r,i-1/2}$ and $F_{r,i-1/2}$

14

as follows:

$$E_{r,i-1/2} = \frac{1}{c}\left(\epsilon^+_{i-1/2} + \epsilon^-_{i-1/2}\right),$$

$$= \frac{E_{r,L,i} + E_{r,R,i-1}}{2} + \frac{\sqrt{3}}{2c}\left(F_{r,R,i-1} - F_{r,L,i}\right), \qquad (2.24)$$

$$F_{r,i-1/2} = \frac{1}{\sqrt{3}}\epsilon^+_{i-1/2} + \frac{-1}{\sqrt{3}}\epsilon^-_{i-1/2},$$

$$= \frac{cE_{r,R,i-1} - cE_{r,L,i}}{2\sqrt{3}} + \frac{1}{2}\left(F_{r,R,i-1} + F_{r,L,i}\right). \qquad (2.25)$$

Because we have 2 equations and 4 unknowns describing the radiation, we can fully determine the system by using both b_L and b_R as test functions in (2.20) and (2.21). We will also use a process called "mass matrix lumping" to improve robustness. To explain this, consider the integral of the time derivative term using both the left and right basis functions. Writing this in matrix form, we have:

$$\begin{bmatrix} \int_{x_{i-1/2}}^{x_{i+1/2}} b_L b_L\, dx & \int_{x_{i-1/2}}^{x_{i+1/2}} b_L b_R\, dx \\ \int_{x_{i-1/2}}^{x_{i+1/2}} b_R b_L\, dx & \int_{x_{i-1/2}}^{x_{i+1/2}} b_R b_R\, dx \end{bmatrix} \begin{bmatrix} \dfrac{\partial E_{r,L}}{\partial t} \\ \dfrac{\partial E_{r,R}}{\partial t} \end{bmatrix} = \Delta x_i \begin{bmatrix} \dfrac{1}{3} & \dfrac{1}{6} \\ \dfrac{1}{6} & \dfrac{1}{3} \end{bmatrix} \begin{bmatrix} \dfrac{\partial E_{r,L}}{\partial t} \\ \dfrac{\partial E_{r,R}}{\partial t} \end{bmatrix}. \qquad (2.26)$$

The matrix on the right-hand side of (2.26) is called a "mass matrix" because it does not involve integrals over the spatial derivatives. In mass matrix lumping, the diagonal of each row is set equal to the sum of the elements of the row, and the off-diagonals are set to zero. For (2.26), this becomes:

$$\Delta x_i \begin{bmatrix} \dfrac{1}{3} & \dfrac{1}{6} \\ \dfrac{1}{6} & \dfrac{1}{3} \end{bmatrix} \begin{bmatrix} \dfrac{\partial E_{r,L}}{\partial t} \\ \dfrac{\partial E_{r,R}}{\partial t} \end{bmatrix} \implies \Delta x_i \begin{bmatrix} \dfrac{1}{2} & 0 \\ 0 & \dfrac{1}{2} \end{bmatrix} \begin{bmatrix} \dfrac{\partial E_{r,L}}{\partial t} \\ \dfrac{\partial E_{r,R}}{\partial t} \end{bmatrix}. \qquad (2.27)$$

Integrating (2.20) and (2.21) using $b_k = b_L$ and incorporating mass matrix lumping, we have:

$$\frac{\Delta x_i}{2} \frac{\partial E_{r,L,i}}{\partial t} + \frac{c}{2\sqrt{3}} \left(E_{r,L,i} - E_{r,R,i-1}\right) + \frac{F_{r,R,i} - F_{r,R,i-1}}{2} = \frac{\Delta x_i}{2} \sigma_{a,L,i} c \left(aT_{L,i}^4 - E_{r,L,i}\right) ,$$

(2.28)

$$\frac{cE_{r,R,i} - cE_{r,R,i-1}}{6} - \frac{F_{r,R,i-1}}{2\sqrt{3}} + \left(\frac{\sigma_{t,L,i}\Delta x_i}{2} + \frac{1}{2\sqrt{3}}\right) F_{r,L,i} = 0 .$$

(2.29)

Likewise, integrating (2.20) and (2.21) using $b_k = b_R$, we have:

$$\frac{\Delta x_i}{2} \frac{\partial E_{r,R,i}}{\partial t} + \frac{c}{2\sqrt{3}} \left(E_{r,R,i} - E_{r,L,i+1}\right) + \frac{F_{r,L,i+1} - F_{r,L,i}}{2} = \frac{\Delta x_i}{2} \sigma_{a,R,i} c \left(aT_{R,i}^4 - E_{r,R,i}\right) ,$$

(2.30)

$$\frac{cE_{r,L,i+1} - cE_{r,L,i}}{6} - \frac{F_{r,L,i+1}}{2\sqrt{3}} + \left(\frac{\sigma_{t,L,i}\Delta x_i}{2} + \frac{1}{2\sqrt{3}}\right) F_{r,L,i} = 0 .$$

(2.31)

We obtain equations for the temperature unknowns in a similar manner, by multiplying (2.16) by a basis function and integrating over the cell width as:

$$\int_{x_{i-1/2}}^{x_{i+1/2}} C_v b_k \frac{\partial T}{\partial t} \, dx = \int_{x_{i-1/2}}^{x_{i+1/2}} b_k \left\{\sigma_a c \left(E - aT^4\right) + Q\right\} \, dx .$$

(2.32)

where $k = L, R$. Carrying out this integration and using mass matrix lumping, we get:

$$C_v \frac{\partial T_{k,i}}{\partial t} = \sigma_{a,k,i} c \left(E_{r,k,i} - aT_{k,i}^4\right) + Q_i .$$

(2.33)

Here, we have a point-wise expression for the temperature unknowns. This preserves the spatial independence of (2.16). Next, we consider the solution at the left and right boundaries.

In our problems, we use source and periodic boundary conditions. Boundary conditions are met by appropriately defining the incident characteristic variables at the boundries:

$$\epsilon_{1/2}^+ = \frac{c}{2} E_{r,L}^{inc} + \frac{\sqrt{3}}{2} F_{r,L}^{inc} , \tag{2.34}$$

$$\epsilon_{N+1/2}^- = \frac{c}{2} E_{r,R}^{inc} - \frac{\sqrt{3}}{2} F_{r,R}^{inc} , \tag{2.35}$$

where $E_{r,L}^{inc}$, $E_{r,R}^{inc}$, $F_{r,L}^{inc}$, and $F_{r,R}^{inc}$ represent the incident values for the left and right values of the radiation energy density and radiation energy flux. For a black-body source condition the incident characteristic variables are set to the correct incident intensity, $acT_{inc}^4/2$, where T_{inc} is the black-body boundary temperature. For example, consider a left boundary black-body source. The characteristic variable is set as follows:

$$\epsilon_{1/2}^+ = \frac{c}{2} E_{r,L}^{inc} + \frac{\sqrt{3}}{2} F_{r,L}^{inc} = \frac{1}{2} acT_{inc}^4 . \tag{2.36}$$

Thus, we have two parameters available, $E_{r,L}^{inc}$ and $F_{r,L}^{inc}$, to determine one value of the incident characteristic variable. For simplicity, we simply choose to set $F_{r,L}^{inc}$ to zero and set $E_{r,L}^{inc} = aT_{inc}^4$.

Periodic boundary conditions are defined such that the radiation energy flux entering the left boundary is equivalent to the energy flux exiting the right boundary and vice versa. This may be written as:

17

$$f^+_{1/2} = f^+_{N+1/2}, \tag{2.37a}$$

$$f^-_{N+1/2} = f^-_{1/2}. \tag{2.37b}$$

Periodic boundary conditions present a challenge to solving our linear system in that the diffusion matrix is no longer banded; thus, solving the system directly would take substantially more computational resources. We can mitigate this by computing the correct periodic boundary conditions in 2x2 system and using those boundary conditions with the standard banded solver to compute the full solution. To compute the periodic boundary conditions, we need to perform three separate diffusion calculations. In the first diffusion solve, we set the incident currents to zero and the distributed source to its actual value and compute the exiting currents, $f^-_{L,1}$ and $f^+_{R,1}$. Then, in the second and third diffusion solves, we set the distributed source to zero, one of the boundaries to an incident current of 1, and the other boundary to 0. We compute the exiting currents for each of these calculations: $f^-_{L,2}$ and $f^+_{R,2}$ when the left boundary is set to 1 and $f^-_{L,3}$ and $f^+_{R,3}$ when the right boundary is set to 1. Then, we set up our 2x2 system as:

$$\begin{bmatrix} f^-_L \\ f^+_R \end{bmatrix} = \begin{bmatrix} f^-_{L,2} & f^-_{L,3} \\ f^+_{R,2} & f^+_{R,3} \end{bmatrix} \begin{bmatrix} f^+_L \\ f^-_R \end{bmatrix} + \begin{bmatrix} f^-_{L,1} \\ f^+_{R,1} \end{bmatrix}. \tag{2.38}$$

Because we're computing periodic boundary conditions, we can relate the inflow currents to the outflow currents as follows:

$$\begin{bmatrix} f^-_L \\ f^+_R \end{bmatrix} = \begin{bmatrix} 0 & 1 \\ 1 & 0 \end{bmatrix} \begin{bmatrix} f^+_L \\ f^-_R \end{bmatrix}. \tag{2.39}$$

Solving this, we have the correct inflow currents to produce the diffusion solution

18

with periodic boundaries. Thus, we only need to perform one more diffusion calculation with f_L^+ and f_R^- to obtain the final solution with periodic boundary conditions for a given iteration.

Substituting (2.34) into (2.24) and (2.25), we obtain equations for the radiation energy density and energy flux at the left boundary:

$$\frac{\Delta x_i}{2}\frac{\partial E_{r,L},1}{\partial t} + \frac{c}{2\sqrt{3}}E_{r,L,1} + \frac{F_{r,R,1}}{2} =$$
$$\frac{\Delta x_i}{2}\sigma_{a,L,1}c\left(aT_{L,1}^4 - E_{r,L,1}\right) + \frac{cE_{r,L}^{inc}}{2\sqrt{3}} + \frac{F_{r,L}^{inc}}{2}, \tag{2.40}$$

$$\frac{cE_{r,R,1}}{6} + \left(\frac{\sigma_{t,L,1}\Delta x_i}{2} + \frac{1}{2\sqrt{3}}\right)F_{r,L,1} = \frac{cE_{r,L}^{inc}}{6} + \frac{F_{r,L}^{inc}}{2\sqrt{3}}. \tag{2.41}$$

Similarly, substituting (2.35) into (2.24) and (2.25), we obtain equations for the solution at the right boundary:

$$\frac{\Delta x_i}{2}\frac{\partial E_{r,R,N}}{\partial t} + \frac{c}{2\sqrt{3}}E_{r,R,N} - \frac{F_{r,L,N}}{2} =$$
$$\frac{\Delta x_i}{2}\sigma_{a,R,N}c\left(aT_{R,N}^4 - E_{r,R,N}\right) + \frac{cE_{r,R}^{inc}}{2\sqrt{3}} - \frac{F_{r,R}^{inc}}{2}, \tag{2.42}$$

$$-\frac{cE_{L,N}}{6} + \left(\frac{\sigma_{t,R,N}\Delta x_i}{2} + \frac{1}{2\sqrt{3}}\right)F_{r,R,N} = -\frac{cE_{r,R}^{inc}}{6} + \frac{F_{r,L}^{inc}}{2\sqrt{3}}. \tag{2.43}$$

Here, we note that (2.33) does not require boundary conditions.

2.3 TR/BDF2 Scheme

The Crank-Nicholson (CN) [8] scheme has been traditionally used in the computational community as a second-order accurate time discretization for radiation transport and diffusion calculations. However, this scheme can yield highly oscil-

latory solutions for stiff systems. The second-order backward difference formula (BDF2) [8] is a one-stage scheme that requires solution values from two previous time steps rather than one (a two-step scheme). It is highly damped and compatible with existing transport acceleration techniques. However, the BDF2 scheme has unusual conservation properties that we consider undesirable. An ideal second-order scheme would possess the following properties:

- one stage,

- one step,

- strong damping of oscillations,

- compatibility with existing transport acceleration techniques,

- standard conservation properties.

We are unaware of any scheme that has all of these properties, but the TR/BDF2 scheme, developed by Bank et. al [2], has all but one. It is a one-step, two-stage algorithm. The solution is computed over a portion of the time step, $\gamma \Delta t$, using the Trapezoid Rule (Crank-Nicholson method); then, the solution over the remainder of the time step, $(1 - \gamma)\Delta t$, is computed using the BDF2 method. To illustrate this, consider the following nonlinear equation:

$$\frac{\partial f}{\partial t} = \mathbf{A}f \, , \tag{2.44}$$

where f is the solution and $\mathbf{A}$ is a nonlinear operator dependent on f. The general TR/BDF2 scheme may be written as:

$$\frac{f^{n+\gamma} - f^n}{\gamma \Delta t} = \frac{1}{2}\left(\mathbf{A}^{n+\gamma}f^{n+\gamma} + \mathbf{A}^n f^n\right) \, , \tag{2.45a}$$

20

$$\frac{(2-\gamma)f^{n+1} - \gamma^{-1}f^{n+\gamma} + \gamma^{-1}(1-\gamma)^2 f^n}{\Delta t} = (1-\gamma)\mathbf{A}^{n+1}f^{n+1} \,. \tag{2.45b}$$

Bank demonstrated that the optimum value of γ is $\sqrt{2}-2$; however, so that the hydro portions of our rad-hydro scheme will be computed over equal time steps, we use use $\gamma = 1/2$. Thus, Eq. (2.45a) and Eq. (2.45b) become:

$$\frac{2(f^{n+1/2} - f^n)}{\Delta t} = \frac{1}{2}\left(\mathbf{A}^{n+1/2}f^{n+1/2} + \mathbf{A}^n f^n\right) \,, \tag{2.46a}$$

$$\frac{3f^{n+1} - 4f^{n+1/2} + f^n}{\Delta t} = \mathbf{A}^{n+1}f^{n+1} \,. \tag{2.46b}$$

We later demonstrate that any advantages in accuracy and stability of the optimal scheme relative to our simplified scheme are negligible.

2.3.1 Conservation

The analytic average value of $\mathbf{A}f$ over a time step is only a function of $\mathbf{A}f$ values evaluated within that step. To demonstrate that a conservation statement may be made for the TR/BDF2 scheme over a single time step, we multiply Eq. (2.46a) by 2, add it to Eq. (2.46b) and divide the sum by 3 to get the following:

$$\frac{f^{n+1} - f^n}{\Delta t} = \frac{1}{3}\left(\mathbf{A}^{n+1}f^{n+1} + \mathbf{A}^{n+1/2}f^{n+1/2} + \mathbf{A}^n f^n\right) \,. \tag{2.47}$$

From Eq. (2.47), we see that the average time derivative of the solution over one time step is equal to a uniform three-point average of $\mathbf{A}f$ over the same time step. Let us now compare this with the standard BDF2 scheme. We demonstrate that the BDF2 scheme fails to preserve this analytic property due to the fact that it is a multistep scheme. One step schemes, like the TR/BDF2 method, have no knowledge of solution values that lie outside of any given time step; thus, additional values cannot appear in the conservation expression. For this demonstration, we use a fixed

time step for simplicity, but the principles we demonstrate apply with arbitrary time steps. Because the BDF2 scheme is a two-step method, we must use a one-step scheme to determine the first time step. Here, we use the Crank-Nicholson scheme. Thus, the solution over the first step is computed using:

$$\frac{f^{(1)} - f^{(0)}}{\Delta t} = \frac{1}{2} \left(\mathbf{A}^{(1)} f^{(1)} + \mathbf{A}^{(0)} f^{(0)} \right) . \tag{2.48}$$

Then, using the standard BDF2 scheme, the solution can be computed at each subsequent time:

$$\frac{3}{2} \frac{f^{n+1} - f^n}{\Delta t} - \frac{1}{2} \frac{f^n - f^{n-1}}{\Delta t} = \mathbf{A}^{n+1} f^{n+1} . \tag{2.49}$$

The partial time derivative of f averaged over $[t^n, t^{n+1}]$ can be expressed for the BDF2 scheme as follows:

$$\frac{f^{n+1} - f^n}{\Delta t} = \frac{1}{3} \frac{f^n - f^{n-1}}{\Delta t} + \frac{2}{3} \mathbf{A}^{n+1} f^{n+1} . \tag{2.50}$$

Using Eq. (2.50) and Eq. (2.48), we find that the conservation expression for the second time step may be written as:

$$\frac{f^{(2)} - f^{(1)}}{\Delta t} = \frac{4}{6} \mathbf{A}^{(2)} f^{(2)} + \frac{1}{6} \mathbf{A}^{(1)} f^{(1)} + \frac{1}{6} \mathbf{A}^{(0)} f^{(0)} . \tag{2.51}$$

Note from the above equation that $\mathbf{A}^{(0)} f^{(0)}$ plays a role in the conservation expression over the time step from $t^{(1)}$ to $t^{(2)}$. Using Eq. (2.50) and Eq. (2.51), we obtain the conservation expression for the third step:

$$\frac{f^{(3)} - f^{(2)}}{\Delta t} = \frac{12}{18} \mathbf{A}^{(3)} f^{(3)} + \frac{4}{18} \mathbf{A}^{(2)} f^{(2)} + \frac{1}{18} \mathbf{A}^{(1)} f^{(1)} + \frac{1}{18} \mathbf{A}^{(0)} f^{(0)} . \tag{2.52}$$

It is not difficult to see from these examples that continued application of Eq. (2.50) yields a conservation statement at each time step that depends upon values of $\mathbf{A}f$ evaluated at each and every previous time. Thus while a conservation expression for each time step can be made with the BDF2 scheme, the resulting expression has an undesirable dependence upon all previously computed values of $\mathbf{A}f$. Nevertheless, if one wishes to compute a conservation statement for the BDF2 scheme for each time step, it can be done fairly efficiently. For instance, if one is only interested in the average value of $\mathbf{A}f$ over the time step, Eq. (2.50) can be directly used. However, it is often of interest to decompose the average of $\mathbf{A}f$ into a sum of component source rates and sink rates. Examples of such components for radiation diffusion include the radiation energy absorption, emission, inflow, and outflow rates. Eq. (2.50) cannot be directly used to compute such components because one does not know how to decompose the terms on the right side of that equation that are functions of f rather than $\mathbf{A}f$. This problem can be circumvented by recognizing that Eq. (2.50) is a recursion formula that relates successive averages of $\mathbf{A}f$. In particular, we can re-express Eq. (2.50) as follows:

$$\langle \mathbf{A}f \rangle^{n+\frac{1}{2}} = \frac{1}{3}\langle \mathbf{A}f \rangle^{n-\frac{1}{2}} + \frac{2}{3}\mathbf{A}^{n+1}f^{n+1}\,, \tag{2.53}$$

where $\langle \mathbf{A}f \rangle^{n+\frac{1}{2}}$ denotes the average value of $\mathbf{A}f$ from t^n to t^{n+1}. One can directly compute the components of $\bar{\mathbf{A}}f$ for the first time step (which must be performed with a one-step scheme), and then use Eq. (2.53) to compute the components for each successive BDF2 step. While Eq. (2.53) only applies with uniform time steps, one can easily compute an analog for arbitrary time steps. The general BDF2 equation

for computing f^{n+1} given f^n and f^{n-1} is

$$\left(\frac{2t^{n+1} - t^n - t^{n-1}}{t^{n+1} - t^{n-1}}\right) \left(\frac{f^{n+1} - f^n}{t^{n+1} - t^n}\right) -$$

$$\left(\frac{t^{n+1} - t^n}{t^{n+1} - t^{n-1}}\right) \left(\frac{f^n - f^{n-1}}{t^n - t^{n-1}}\right) = \mathbf{A}^{n+1} f^{n+1}. \tag{2.54}$$

2.3.2 Accuracy

Next, to demonstrate accuracy and stability, consider the following linear ODE:

$$\frac{\partial f}{\partial t} + kf = 0 \quad , f(0) = 1,\ k > 0. \tag{2.55}$$

Applying Eqs. (2.46a) and ((2.46b)) to the ODE in Eq. (2.55), we get the following solution for f^{n+1}:

$$f^{n+1} = \frac{12 - 5z}{12 + 7z + z^2} f^n. \tag{2.56}$$

where $z = k\Delta t$. By performing a Taylor series expansion on Eq. (2.56) and comparing that with a Taylor series expansion of the exact solution, $f(t) = exp(-z)$, we see that the expression in Eq. (2.56) is locally third-order accurate:

$$f^{n+1} = e^{-z} - \frac{1}{24}(z^3). \tag{2.57}$$

Thus, the method is globally second-order accurate. The leading-order coefficient for the optimal TR/BDF2 method is $-\left(\frac{1}{\sqrt{3}} - \frac{2}{3}\right) \approx -0.0404$ which is negligibly smaller in magnitude than $-\frac{1}{24} \approx -0.0417$. Thus the difference in truncation error between the two methods is negligible.

2.3.3 Stability

As shown in Fig. 2.1, by plotting the amplification factor that relates f^n to f^{n+1} in Eq. (2.56), we can observe the stability of the method as a function of z. We can see that the function has a maximum value of 1, a minimum value of -0.212, and approaches zero as z approaches infinity; thus, the TR/BDF2 method is L-stable. Furthermore, though the method can oscillate, oscillatory modes will be damped by about 80 percent at each time step. This is much better behavior than the Crank-Nicholson scheme, which is not L-stable and has a minimum value of -1 so that oscillatory modes may not be damped at all. The optimal TR/BDF2 method has a minimum amplification factor of -.207, which is negligibly better than that of the simplified TR/BDF2 value.

2.3.4 Connection to Runge-Kutta Methods

The general TR/BDF2 scheme can be categorized as an implicit Runge-Kutta method. For instance, an s-stage Runge-Kutta method for solving the nonlinear equation

$$\frac{\partial f}{\partial t} = G(t, f),\tag{2.58}$$

can be expressed in terms of the $s \times s$ matrix B, and the s-vectors c and d as follows:

$$F_i = f^n + \Delta t \sum_{j=1}^{s} b_{i,j}\, G\left(t^n + c_j \Delta t, F_j\right), \quad i = 1, \ldots, s.\tag{2.59}$$

$$f^{n+1} = f^n + \Delta t \sum_{i=1}^{s} d_i\, G\left(t^n + c_i \Delta t, F_i\right).\tag{2.60}$$
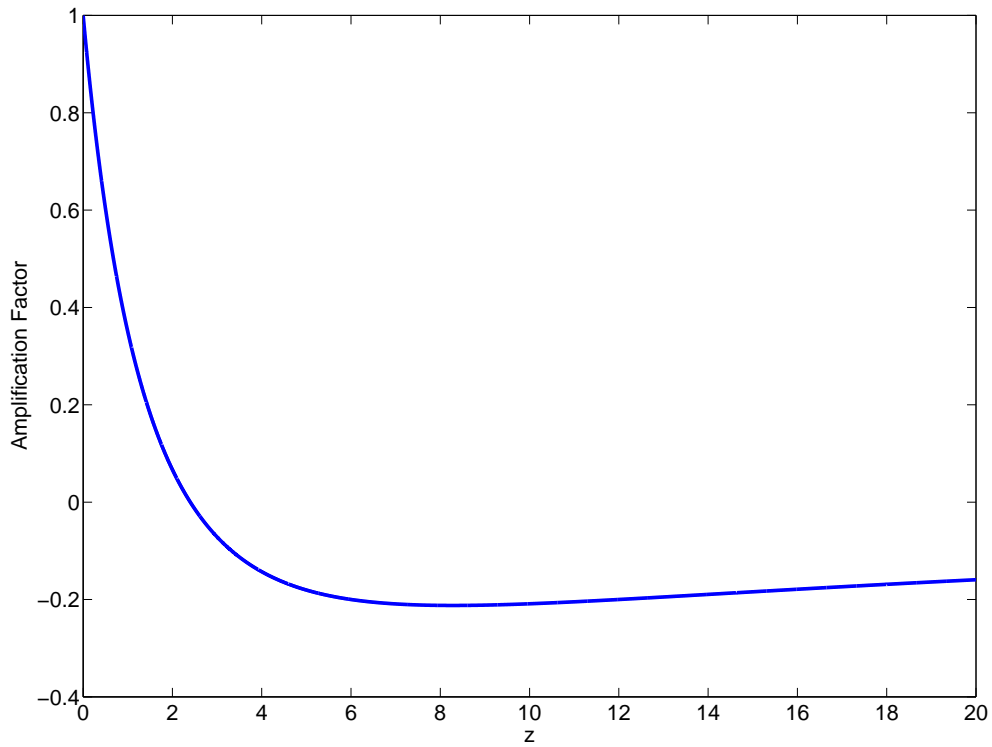
Figure 2.1: Stability curve for the TR/BDF2 scheme.

This information can be conveniently expressed using a Butcher tableau:

$$
\begin{array}{c|c}
c & B \\
\hline
 & d^T
\end{array}
\tag{2.61}
$$

The tableau for the general TR/BDF2 scheme (which requires considerable algebraic

manipulation of Eqs. ((2.45a)) and ((2.45b)) to obtain) is

$$
\begin{array}{c|ccc}
0 & 0 & 0 & 0 \\
\gamma & \gamma/2 & \gamma/2 & 0 \\
1 & 1/[2(2-\gamma)] & 1/[2(2-\gamma)] & (1-\gamma)/(2-\gamma) \\
\hline
 & 1/[2(2-\gamma)] & 1/[2(2-\gamma)] & (1-\gamma)/(2-\gamma)
\end{array}
\tag{2.62}
$$

Note from the tableau that this scheme has three stages. However, because F_1, is equal to f^n one need not solve an equation to obtain it. Schemes with this property are referred to as FSAL (First-Same as Last). In Section 1 we noted that the two equations that must be solved each time step in the general TR/BDF2 method can be solved sequentially rather than simultaneously. This property is expressed in the tableau by the lower-triangular structure of B. Schemes with this property are referred to as Diagonally-Implicit-Runge-Kutta schemes.

In the following section, we will consider several variations on the TR/BDF2 scheme for solving non-linear systems. We will test both fully converged and single-iteration Newton and Picard schemes applied to our radiative diffusion system and compare the results for both accuracy and efficiency.

3.   VARIATIONS ON THE TR/BDF2 SCHEME*

In this section, we apply several variations of the TR/BDF2 method to the 1D, grey equations of nonlinear radiative heat diffusion and compare their performance with the more widely-used Crank-Nicholson scheme. This radiative heat diffusion system is equivalent to the implicit component of our radiation-hydrodynamics model, given by Eq. (2.5), in a static medium. Because these equations are nonlinear, we examine various treatments for the nonlinear terms. Traditionally, the Newton method is used to solve these equations. However, because photon cross-section data is generally tabular, the contributions to the Jacobian matrix from the cross-sections are usually neglected, resulting in a kind of hybrid Newton-Picard method. We examine the cost of the Newton-Picard method in terms of both accuracy and efficiency relative to the pure Newton method. We also compare the efficiency obtained by converging the nonlinear terms with that obtained by fixing the number of iterations. The study presented here, which was previously published in [7], is somewhat similar to that of Lowrie [19] except that he considered variations of the Crank-Nicholson scheme rather than the TR/BDF2 scheme. The results of this analysis, in turn, inform our decision on how to implement the TR/BDF2 method into our overall radiation-hydrodynamics algorithm.

In the remainder of this section, we develop our variants on the TR/BDF2 scheme which we later apply to the radiative heat diffusion equations. We describe the two problems we use to test our methods - a smooth, sinusoidal problem and a Marshak wave, and show the results for each before presenting our conclusions.

3.1 Radiative Heat Diffusion Equations

The radiative heat diffusion equations describe how heat is exchanged via photon emission and absorption in a static medium with the assumption that the angular distribution of the radiation is linear. We further assume a 1-D, grey model for radiation energy density. The equations describing this system are:

$$\frac{\partial E_r}{\partial t} + \frac{\partial F_r}{\partial x} = \sigma_a c \left(a T^4 - E_r \right) , \tag{3.1a}$$

$$\frac{1}{3}\frac{\partial E_r}{\partial x} + \frac{\sigma_t}{c} F_r = 0 , \tag{3.1b}$$

$$C_v \frac{\partial T}{\partial t} = \sigma_a c \left(E_r - a T^4 \right) . \tag{3.1c}$$

The dependent variables in these equations, E_r and T, represent radiation energy density and material temperature, respectively. The absorption and total cross sections, σ_a and σ_t, both strongly depend on temperature, but because the heat capacity, C_v, only weakly depends on T, we treat it as constant. Lastly, a and c represent the Boltzmann constant and the speed of light. In space, these equations are discretized using an LDG scheme, which is second-order accurate.[33, 34] These equations are solved by first linearizing Eqs. (3.1a) and ((3.1c)) using one of two methods described in a later section. Then, the linearized version of Eq. (3.1c) is used to eliminate the implicit temperature terms from Eq. (3.1a) resulting in a diffusion equation implicitly dependent only on E_r. Due to the relatively few number of unknowns used in our problems, this equation is solved directly using Gauss elimination. Finally, using E_r and Eq. (3.1c), the temperature is computed locally.

29

3.2 Variations on the TR/BDF2 Method

Here, we describe our variations on the TR/BDF2 scheme. They differ according to our treatment of the cross sections and whether the solution is converged or the number of iterations fixed.

To ensure stability, the Planck function is always treated via the Newton method. We treat the cross-sections using two types of iteration schemes. The first is the Newton method, which requires temperature derivatives of the cross-sections and converges quadratically once the iterate is sufficiently close to the solution.[29] The second iteration scheme is Picard's method (also known as fixed-point iteration) which does not require temperature derivatives of the cross sections but converges linearly once the iterate is sufficiently close to the solution.[29] For simplicity, we define our methods in terms of Eq. (2.44). When it is necessary, the operator $\mathbf{A}$ is expressed as a product of two matrices, $\mathbf{B}$ and $\mathbf{C}$, where the former represents those components of $\mathbf{A}$ containing cross sections and the latter represents those containing the Planck function. Our system cannot actually be expressed in this form, but we assume that it can be so expressed as a simple device for making the treatment of the cross sections and the Planck function apparent without consideration of the full equations. The operators in our descriptions carry iteration information in addition to time indexing. Quantities evaluated at the previous iterate carry a superscript "*". For instance, f^* denotes the previous iterate for f. The primary unknown in each equation takes the form of δf, the additive change in the iterate for f. For instance, the new iterate of f is given by $\delta f + f^*$.

3.2.1 Converged Newton Method

The first variation is to apply the Newton method to both the cross sections and the Planck function.

30

$$\frac{2\left(\delta f + f^* - f^n\right)}{\Delta t} = \frac{1}{2}\left(\mathbf{A}^*\left(\delta f + f^*\right) + \frac{\partial \mathbf{A}^*}{\partial f} f^*\delta f + \mathbf{A}^n f^n\right). \qquad \text{(3.2a)}$$

Note that f^* denotes the previous iteration value for $f^{n+\frac{1}{2}}$ in the above equation. The initial value for f^* is f^n. The iteration process is converged for the above equation before proceeding to the next equation.

$$\frac{3\left(\delta f + f^*\right) - 4f^{n+\frac{1}{2}} + f^n}{\Delta t} = \mathbf{A}^*\left(\delta f + f^*\right) + \frac{\partial \mathbf{A}^*}{\partial f} f^*\delta f. \qquad \text{(3.2b)}$$

Note that f^* denotes the previous iteration value for f^{n+1} in the above equation. The initial value for f^* is $f^{n+\frac{1}{2}}$.

3.2.2   One-Iteration Newton Method

Another option is to stop iterating after a single iteration of the converged Newton method:

$$\frac{2\delta f}{\Delta t} = \frac{1}{2}\left(\mathbf{A}^n\left(\delta f + f^n\right) + \frac{\partial \mathbf{A}^n}{\partial f} f^n\delta f + \mathbf{A}^n f^n\right). \qquad \text{(3.3a)}$$

$$\frac{3\left(\delta f + f^{n+\frac{1}{2}}\right) - 4f^{n+\frac{1}{2}} + f^n}{\Delta t} =$$
$$\mathbf{A}^{n+1/2}\left(\delta f + f^{n+\frac{1}{2}}\right) + \frac{\partial \mathbf{A}^{n+\frac{1}{2}}}{\partial f} f^{n+\frac{1}{2}}\delta f. \qquad \text{(3.3b)}$$

3.2.3   Converged Hybrid Method

The next variation is to treat the cross sections using Picard's method. This is similar to the Newton method, except that the contribution from the derivatives of

the cross sections to the Jacobian are neglected:

$$\frac{2\left(\delta f + f^* - f^n\right)}{\Delta t} =$$
$$\frac{1}{2}\left[\mathbf{B}^*\left(\mathbf{C}^*\left(\delta f + f^*\right) + \frac{\partial \mathbf{C}^*}{\partial f}\, f^* \delta f\right) + \mathbf{B}^n \mathbf{C}^n f^n\right]. \tag{3.4a}$$

Note that f^* denotes the previous iteration value for $f^{n+\frac{1}{2}}$ in the above equation. The initial value for f^* is f^n. The iteration process is converged for the above equation before proceeding to the next.

$$\frac{3\left(\delta f + f^*\right) - 4 f^{n+\frac{1}{2}} + f^n}{\Delta t} = \mathbf{B}^*\left(\mathbf{C}^*\left(\delta f + f^*\right) + \frac{\partial \mathbf{C}^*}{\partial f}\, f^* \delta f\right). \tag{3.4b}$$

Note that f^* denotes the previous iteration value for f^{n+1} in the above equation. The initial value for f^* is $f^{n+\frac{1}{2}}$.

It should be noted that the Newton method and the hybrid method converge to the same solution, but the hybrid method will generally be expected to require more iterations to converge.

3.2.4   Two-Iteration Hybrid Method

The last variant is a two-iteration hybrid method. Because Picard's method is used to treat the cross sections, the additional iteration is necessary to achieve second order-accuracy.

$$\frac{2\left(\delta f\right)}{\Delta t} =$$
$$\frac{1}{2}\left[\mathbf{B}^n\left(\mathbf{C}^n\left(\delta f + f^n\right) + \frac{\partial \mathbf{C}^n}{\partial f}\, f^n \delta f\right) + \mathbf{B}^n \mathbf{C}^n f^n\right]. \tag{3.5a}$$

$$f^* = \delta f + f^n. \tag{3.5b}$$

$$\frac{2\left(\delta f + f^* - f^n\right)}{\Delta t} =$$
$$\frac{1}{2}\left[\mathbf{B}^*\left(\mathbf{C}^*\left(\delta f + f^*\right) + \frac{\partial \mathbf{C}^*}{\partial f} f^*\delta f\right) + \mathbf{B}^n\mathbf{C}^n f^n\right]. \tag{3.5c}$$

$$f^{n+\frac{1}{2}} = \delta f + f^*. \tag{3.5d}$$

$$\frac{3\left(\delta f + f^{n+\frac{1}{2}}\right) - 4f^{n+\frac{1}{2}} + f^n}{\Delta t} =$$
$$\mathbf{B}^{n+\frac{1}{2}}\left(\mathbf{C}^{n+\frac{1}{2}}\left(\delta f + f^{n+\frac{1}{2}}\right) + \frac{\partial \mathbf{C}^{n+\frac{1}{2}}}{\partial f} f^{n+\frac{1}{2}}\delta f\right). \tag{3.5e}$$

$$f^* = \delta f + f^{n+\frac{1}{2}}. \tag{3.5f}$$

$$\frac{3\left(\delta f + f^*\right) - 4f^{n+\frac{1}{2}} + f^n}{\Delta t} =$$
$$\mathbf{B}^*\left(\mathbf{C}^*\left(\delta f + f^*\right) + \frac{\partial \mathbf{C}^*}{\partial f} f^*\delta f\right). \tag{3.5g}$$

$$f^{n+1} = \delta f + f^*. \tag{3.5h}$$

3.3 Computational Results

In this section we present our computational results. Two problems are considered and both accuracy and efficiency are measured.

3.3.1 Infinite Medium Sine Wave Problem

The first of our test problems is an infinite medium sine wave. Because the solution is infinitely differentiable in space and time, this problem is designed to show asymptotic behavior quickly. The initial radiation energy density is defined as:

$$E_r(x) = 0.05 + \frac{1 - 0.05}{2}\left[1 + \sin\left\{\frac{\pi}{2}\frac{2x - 0.05}{0.05}\right\}\right], \tag{3.6}$$

33

which varies monotonically from 0.05 to 1.0 jerks/cm^3. We apply reflective boundary conditions so that our problem represents a continous sine wave in an infinite medium. The temperature is set to be in thermal equilibrium with the material, i.e. $E_r = aT^4$. As the sine wave evolves toward the final time of 0.02 shakes, it will relax monotonically, approaching a constant solution as $t \to \infty$. The cross sections have the following temperature dependence:

$$\sigma_a(T) = \frac{\sigma_o}{T^3} \, , \tag{3.7}$$

where σ_o is a constant equal to 0.3, and $\sigma_t(T) = \sigma_a(T)$. The spatial domain is a 0.05 cm thick slab discretized into 50 spatial cells, and the heat capacity, C_v , is 0.3 jerks/(cm^3 keV). We use fixed time steps and converge the solution to a relative tolerance of 10^{-8}, where the tolerance, ϵ, is given by:

$$\epsilon = \max_i \frac{2|\phi_i^{k+1} - \phi_i^k|}{\phi_i^{k+1} + \phi_i^k} \tag{3.8}$$

and ϕ_i^k represents one of the cell-averaged conserved variables in cell i at iteration k.

3.3.1.1   Accuracy

To compare our TR/BDF2 schemes, we run this problem varying the number of time steps from 1K to 64K. We compute the error for each method by comparing it with a numerical "exact" solution at the final time of the calculation. This is generated using the converged Newton TR/BDF2 scheme with 1024K time steps, which is 16 times more refined than the smallest tested time step. The error is computed as:

$$e_{\phi,\Delta t} = \frac{\|\phi_{\Delta t} - \phi_{exact}\|_2}{\|\phi_{exact}\|_2} \, , \tag{3.9}$$

where ϕ is either E_r or T. For comparison, in addition to the TR/BDF2 based schemes described in Section 3.2, we include results generated using the Crank Nicholson scheme. For these two additional methods, we use the converged Newton approach to treat the nonlinearities. Figs. 3.1 and 3.2 show the error as a function of the number of time steps for the radiation energy density and material temperature, respectively.
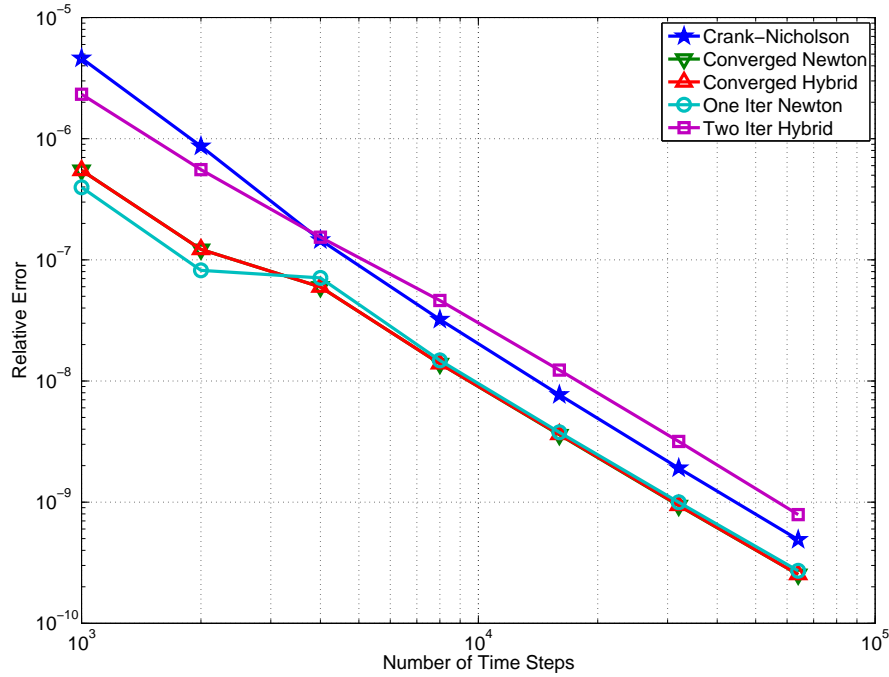

Figure 3.1: Error in radiation energy density versus number of time steps for the infinite medium sine wave.

From these pictures, we can see that the converged TR/BDF2 schemes are the most accurate. Furthermore, as the time step becomes small, the one-iteration New-
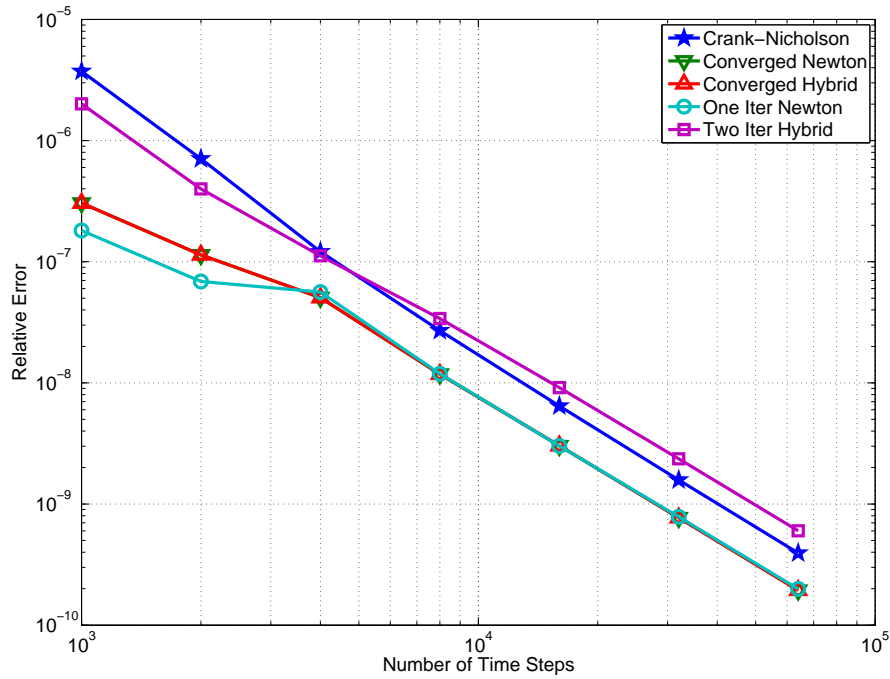
Figure 3.2: Error in temperature versus number of time steps for the infinite medium sine wave.

ton method has the same error as the fully converged methods. So, for the infinite medium sine wave problem, as we increase the number of time steps past 4000, one Newton iteration is sufficient to reduce the error associated with convergence below the error of the TR/BDF2 method itself. We can also see that these three TR/BDF2 methods are roughly twice as accurate as the Crank Nicholson method and six times as accurate as the two-iteration hybrid scheme.

To determine order-accuracy, we perform linear-regression analysis on the error data. Table 3.1 shows the results of this analysis for each method using the portion of the data showing asymptotic behavior.

Table 3.1: Computed orders of accuracy for the infinite medium sine wave.

Method	Radiation Energy Density	Temperature
Crank-Nicholson	2.05	2.06
Converged Newton TR/BDF2	1.97	2.00
One-Iteration Newton TR/BDF2	2.00	2.02
Converged Hybrid TR/BDF2	1.97	2.00
Two-Iteration Hybrid TR/BDF2	1.91	1.89

3.3.1.2   Efficiency

Accuracy is not the only characteristic of interest; we also want to determine the efficiency of each method. We define efficiency as follows:

$$\epsilon_{\phi,\Delta t} = \frac{1}{e_{\phi,\Delta t} W_{\Delta t}} \, , \tag{3.10}$$

where $W_{\Delta t}$ is the total number of iterations for the entire calculation, each roughly equivalent to one iteration of Crank-Nicholson. Thus, the efficiency is a measure of the error reduction per unit work, and the optimal method has the highest efficiency. Figs. 3.3 and 3.4 show the efficiencies of the radiation energy density and temperature for the infinite medium sine wave, respectively.

In each of these figures, we can see that the one-iteration Newton scheme is twice as efficient as the converged schemes. Moreover, it is roughly an order of magnitude more efficient than the two-iteration hybrid scheme.

3.3.2   Marshak Wave

The next test is a Marshak wave, which is designed to compare the methods using a more realistic problem. Here, we use a constant initial temperature of .001 keV throughout the interior of the problem with a 1 keV source at the left boundary. The right boundary is a vacuum, and again, the radiation energy density and material
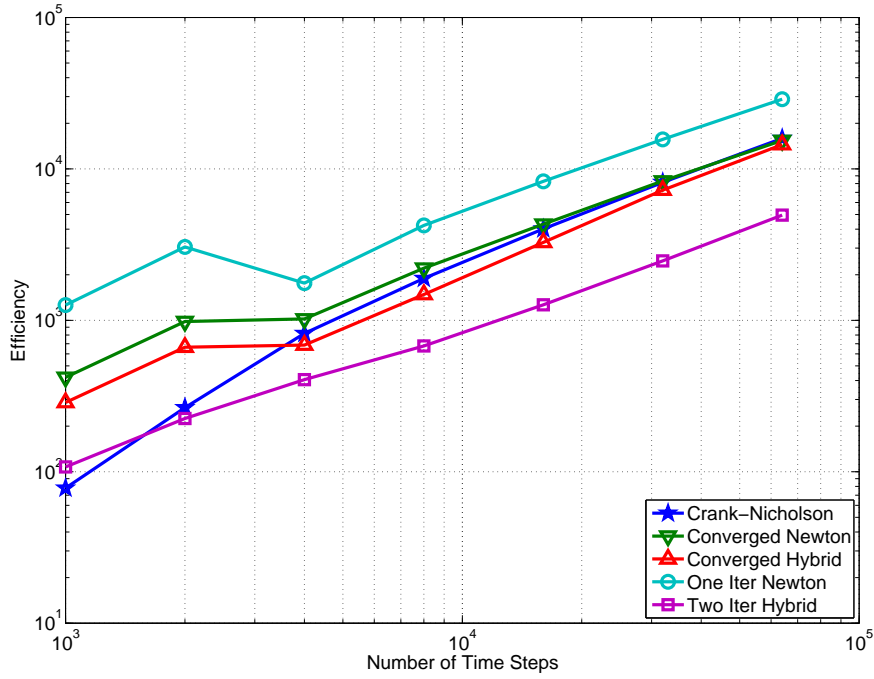
Figure 3.3: Efficiency of the methods for radiation energy density versus number of time steps for the infinite medium sine wave.

temperature are in thermal equilibrium. t_{fin} is 0.1 shake, and $\sigma_o = 300$. Fig. 3.5 shows the radiation and material temperatures at the final time, where the radiation temperature is defined as:

$$T_R = \sqrt[4]{E/a} \,. \tag{3.11}$$

3.3.2.1   Time Step Control

For this problem, we use a variable time step control scheme based on a user-specified "target temperature change", ΔT_{targ}. For a given time step, the maximum
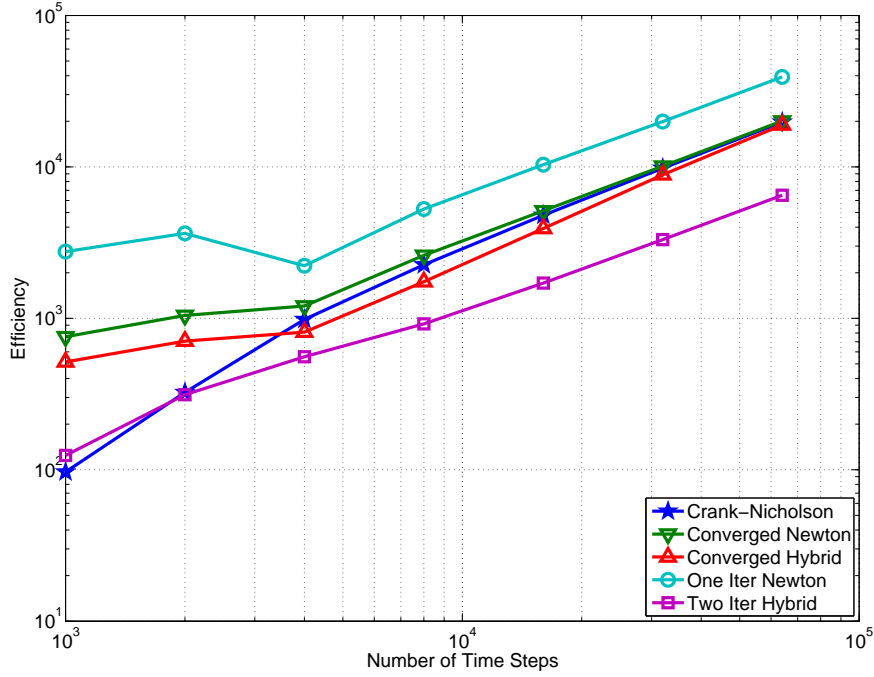
Figure 3.4: Efficiency of the methods for temperature versus number of time steps for the infinite medium sine wave.

relative change is computed using:

$$\Delta T = 2 \max_i \frac{|T_i^{n+1} - T_i^n|}{T_i^{n+1} + T_i^n} \; . \tag{3.12}$$

This result is compared with the target temperature change to determine the next time step:

$$\Delta t^{n+1/2} = \min\left(\frac{\Delta T_{targ}}{\Delta T} \Delta t^{n-1/2}, t - t_{fin}\right) \; . \tag{3.13}$$

The second term forces the final time step to end the calculation at t_{fin}. Also, in order to ensure that the temperature doesn't vary too much, ΔT is also compared with a maximum allowed temperature change, ΔT_{max}. If $\Delta T > \Delta T_{max}$, then the
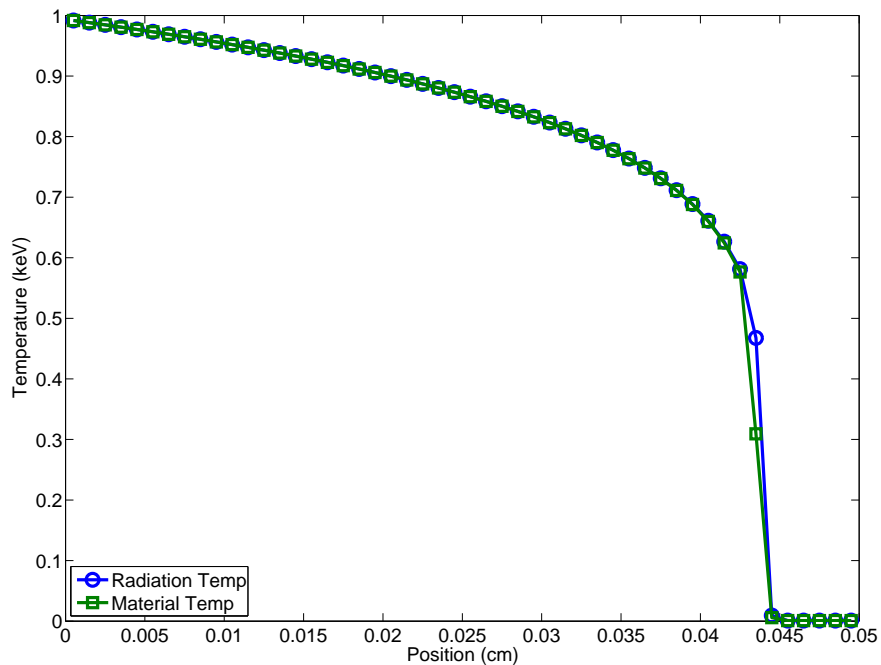
Figure 3.5: Final solution of Marshak wave problem.

time step $\Delta t^{n+1/2}$ is reduced by a factor of $1/3$, and the calculation is repeated from t_n. In our calculations, we set $\Delta T_{max} = 1.2 \Delta T_{targ}$.

3.3.2.2 Accuracy

We run this problem varying the target temperature change from 1% to 20% and converging the solution to a relative tolerance of 10^{-4}. The exact solution is computed using one million fixed time steps, i.e. $\Delta t_{exact} = 10^{-7}$ shakes, which is the minimum time step allowed in our calculations. The exact solution uses roughly 30 times more time steps than the 1% target calculation. Figs. 3.6 and 3.7 show the error in radiation energy density and temperature, respectively, for the Marshak wave.
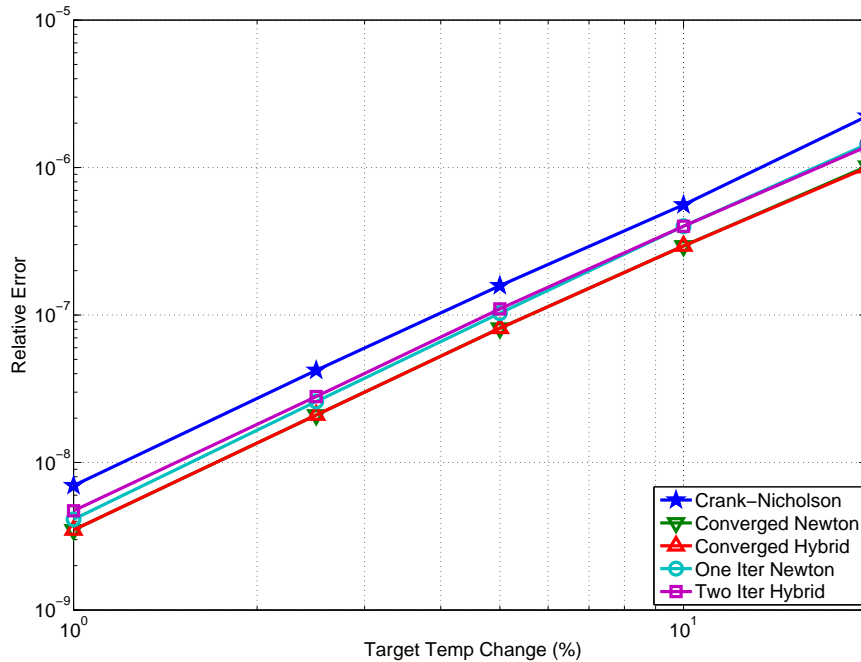
Figure 3.6: Error in radiation energy density versus number of time steps for the Marshak wave.

Again, we see that the converged TR/BDF2 schemes are the most accurate by about a factor of 2. Furthermore, because the one-iteration scheme is never quite as accurate as the converged schemes, we see some benefit to converging the nonlinear terms in this problem. Though this problem is rapidly varying at the wavefront, we still see asymptotic behavior in the error allowing us to compute the order-accuracy of each method, shown in Table 3.2.

3.3.2.3   Efficiency

As with the infinite medium sine problem, we also compare the efficiencies of each method for the Marshak wave. Figs. 3.8 and 3.9 show these efficiencies for radiation energy and material temperature.
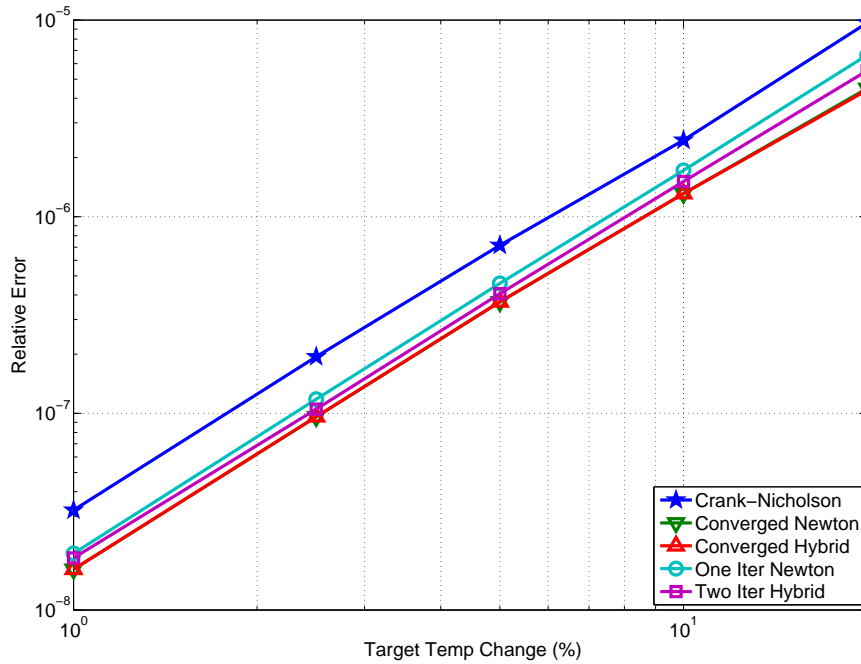
Figure 3.7: Error in temperature versus number of time steps for the Marshak wave.

From these figures we can see that the one-iteration Newton method is, again, twice as efficient as any other scheme. In this case, however, the two-iteration hybrid method is also more efficient than the converged schemes. This is a result of the extra effort required to converge the nonlinear terms when the solution is rapidly varying.

3.3.3   The Maximum Principle

There is one advantage to fully converging the nonlinearities that we have not discussed because it did not arise in our test problems. This relates to the preservation of the thermodynamic maximum principle. This principle is quite simple and can be characterized as follows. Given a closed thermodynamic system with an ini-

Table 3.2: Computed orders of accuracy for the Marshak wave.

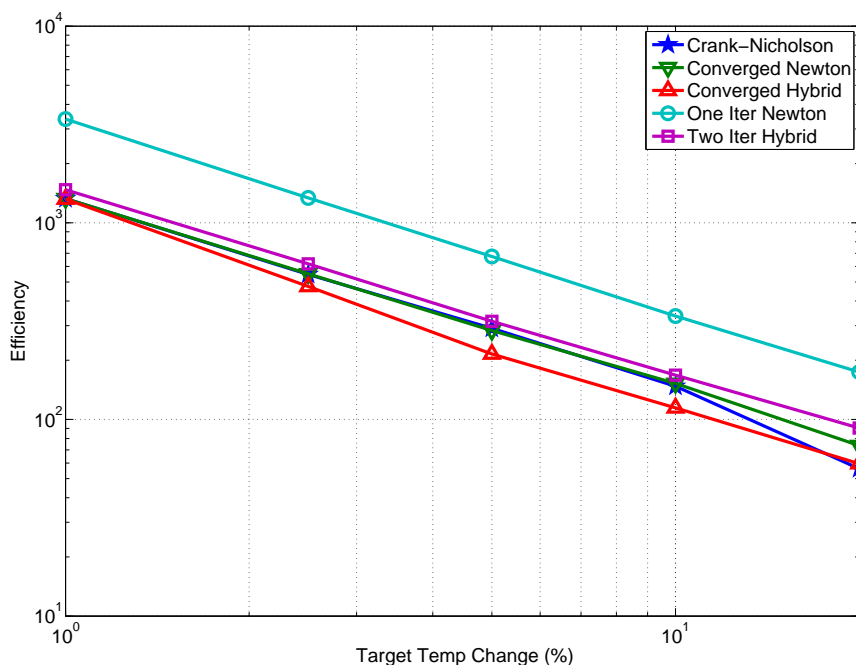| Method	Radiation Energy Density	Temperature
Crank-Nicholson	1.93	1.91
Converged Newton TR/BDF2	1.92	1.90
One-Iteration Newton TR/BDF2	1.98	1.97
Converged Hybrid TR/BDF2	1.92	1.90
Two-Iteration Hybrid TR/BDF2	1.92	1.93

Figure 3.8: Efficiency of the methods for radiation energy density versus number of time steps for the Marshak wave.

tial temperature distribution and no inhomogeneous or external energy sources, the temperature must evolve such that the temperature at any point never exceeds the maximum initial temperature in the system. It has been observed that this prin-
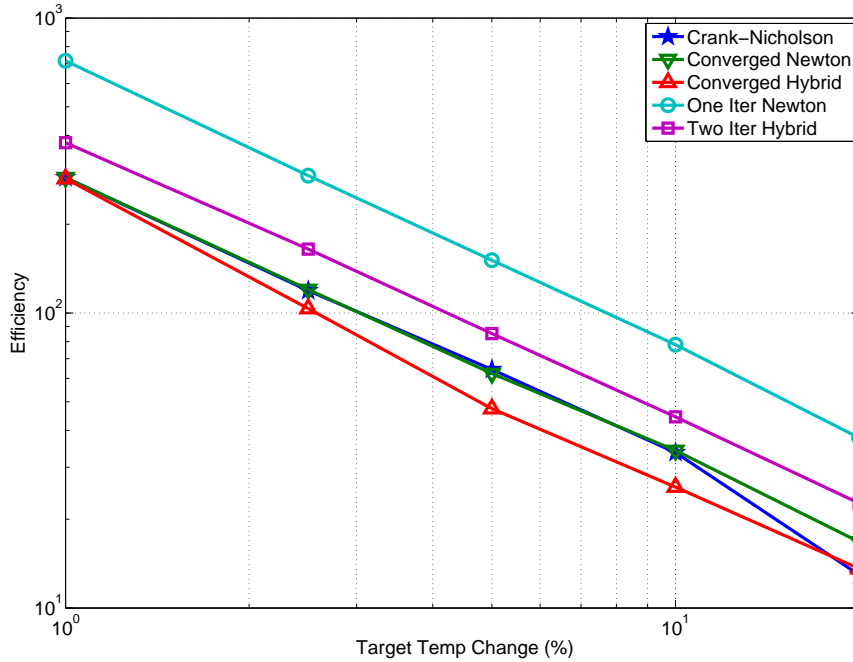
Figure 3.9: Efficiency of the methods for temperature versus number of times teps for the Marshak wave.

ciple can be violated with sufficiently large time steps if the nonlinearities are not converged [11]. To our knowledge, this effect has not been theoretically analyzed except in case of the implicit Monte Carlo method where the nonlinearities are never converged [13]. For example, in the Marshak wave problem, neither the radiation temperature nor the material temperature should exceed the boundary radiation temperature of 1 keV. We performed the Marshak problem with a fixed time step of 2×10^{-4} sh using both the one-iteration Newton method and the converged Newton method. The material temperature solutions after two time steps are compared for these two methods in Fig. 3.10. The one-iteration Newton solution clearly violates the maximum principle, but the converged Newton solution does not. This effect

does not appear when our time step control algorithm is used, presumably because the time steps are sufficiently small to avoid it. Nonetheless this is an effect that should generally be kept in mind when choosing a time-integration scheme.
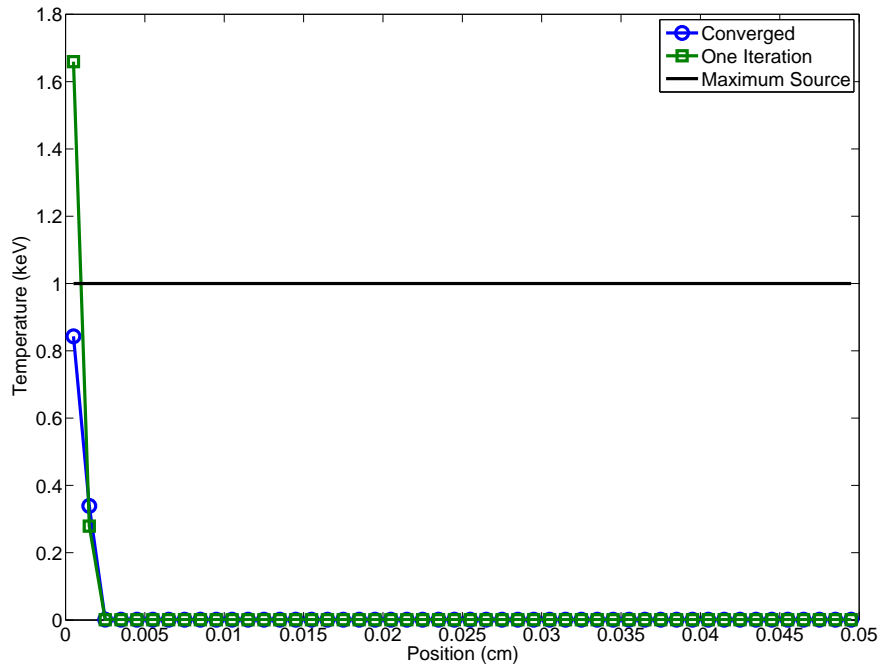
Figure 3.10: Material temperature solutions after two time steps for the Marshak wave problem with fixed time steps of 2×10^{-4} sh.

3.4   Conclusions

The TR/BDF2 method meets the qualifications that we outlined, and thus appears to be a valuable alternative for solving the nonlinear radiative heat diffusion equations. In each of the test problems, we find that the converged TR/BDF2 schemes are consistently the most accurate, and the one-iteration Newton TR/BDF2

scheme is always the most efficient. This result is in basic agreement with [19], which also shows the one-iteration Newton variant to be the most efficient treatment of the nonlinear terms. We can see that the cost of neglecting the temperature derivatives of the cross sections can reduce efficiency by at least one half and as much as an order of magnitude. For the smooth test problem, the converged hybrid method is not only more accurate but is also more efficient than its fixed iteration alternative. However, for the Marshak wave problem, the two-iteration hybrid scheme has superior efficiency to both the converged Newton and hybrid schemes.

Given these results, we choose the converged hybrid method for our radiation-hydrodynamics algorithm. This method will give us the highest level of accuracy while still being easily applicable to both continuous and tabular cross-section data. Furthermore, as previously noted, converging the nonlinearities is required to preserve the maximum principle independently of the time step size.

4. OUR SECOND-ORDER ACCURATE RADIATION-HYDRODYNAMICS METHOD

Our radiation-hydrodynamics scheme consists of two cycles, each of which includes a full MHM step to compute the material advection components, an explicit update for radiation momentum deposition to the fluid, and an implicit solve to compute the radiation diffusion and material energy exchange. In the first cycle, the radiation solve is computed using the Crank-Nicholson scheme, and in the second cycle, the radiation solve is computed using the BDF2 scheme. An outline of our two-cycle system is given as follows:

Cycle 1

1. Reconstruct hydro unknowns at t^n from cell averages.

2. Evolve fluid by $1/4 \, \Delta t$.

3. Update 1/4 step momentum using explicit radiation quantities at t^n.

4. Iterate until 1/4 step values are converged.

   (a) Crank-Nicholson calculation to compute $E_r^{n+1/4}$ and $F_r^{n+1/4}$.

   (b) Crank-Nicholson calculation to update $E^{n+1/4}$ to include effects of radiation/material energy exchange.

5. Reconstruct hydro unknowns at $t^n + 1/4$ from cell averages.

6. Compute advection fluxes at $t^n + 1/4$ using a Riemann solver and $t^{n+1/4}$ hydro unknowns.

7. Advect density, momentum, and material energy from t^n by $1/2$ Δt using $t^n + 1/4$ fluxes.

8. Update $1/2$ step momentum using explicit radiation quantities at $t^{n+1/4}$.

9. Restore LD slopes to internal energy.

10. Iterate until $1/2$ step values are converged.

   (a) Crank-Nicholson calculation to compute $E_r^{n+1/2}$ and $F_r^{n+1/2}$

   (b) Crank-Nicholson calculation to update $E^{n+1/2}$ to include effects of radiation momentum deposition and energy exchange.

Cycle 2

1. Reconstruct hydro unknowns at $t^n + 1/2$ from cell averages.

2. Evolve fluid by $1/4$ Δt.

3. Update $3/4$ step momentum using explicit radiation quantities at $t^{n+1/2}$.

4. Iterate until $3/4$ step values are converged.

   (a) Crank-Nicholson calculation to compute $E_r^{n+3/4}$ and $F_r^{n+3/4}$.

   (b) Crank-Nicholson calculation to update $E^{n+3/4}$ to include effects of radiation kinetic energy deposition and radiation energy exchange.

5. Reconstruct hydro unknowns at $t^n + 3/4$ from cell averages.

6. Compute advection fluxes at $t^n + 3/4$ using a Riemann solver and $t^{n+3/4}$ hydro unknowns.

7. Advect density, momentum, and material energy from $t^n + 1/2$ by $1/2$ Δt using $t^n + 3/4$ fluxes.

48

8. Compute full step momentum using explicit radiation quantities at $t^{n+1/2}$ and fluid fluxes at $t^{n+1/4}$ and $t^{n+3/4}$.

9. Restore LD slopes to internal energy.

10. Iterate until full step values are converged.

    (a) BDF2 calculation to compute E_r^{n+1} and F_r^{n+1}

    (b) BDF2 calculation to update E^{n+1} to include effects of radiation momentum deposition and energy exchange.

4.1   Cycle 1

In this section, we define the first cycle of our hybrid MUSCL-Hancock TR/BDF2 scheme in further detail. We begin our IMEX scheme by linearly reconstructing the hydro unknowns, U_i^n:

$$U_{L,i}^n = U_i^n - \frac{\Delta_i^n}{2}; \quad U_{R,i}^n = U_i^n + \frac{\Delta_i^n}{2}, \tag{4.1}$$

where

$$U_i = \begin{bmatrix} \rho_i \\ (\rho u)_i \\ E_i \end{bmatrix}, \tag{4.2}$$

and Δ_i is some slope constructed from the cell-centered data. Next, we evolve the hydro unknowns over a quarter time-step:

$$U_i^* = U_i^n + \frac{\Delta t}{4\Delta x} \left(F_{L,i}^n - F_{R,i}^n \right), \tag{4.3}$$

where $F_{L/R,i}$ is the hydro flux computed as $F(U_{L/R,i})$. Note that $\rho_i^{n+1/4} = \rho_i^*$. We

continue by updating the fluid momentum in the predictor with the cell-averaged, explicit radiation momentum deposition:

$$\frac{4\rho_i^{n+1/4}\left(u_i^{n+1/4} - u_i^*\right)}{\Delta t} = \frac{1}{2}\frac{\sigma_{t,L,i}^n}{c}\left(F_{r,L,i}^n - \frac{4}{3}E_{r,L,i}^n u_{L,i}^n\right)$$
$$+ \frac{1}{2}\frac{\sigma_{t,R,i}^n}{c}\left(F_{r,R,i}^n - \frac{4}{3}E_{r,R,i}^n u_{R,i}^n\right) . \tag{4.4}$$

Then, we perform our nonlinear iterations for the predictor, in which we implicitly solve for the radiation energy density and current and update the material energy using the Crank-Nicholson method:

$$\frac{4\left(E_r^{n+1/4,k+1} - E_r^n\right)}{\Delta t} = -\frac{1}{2}\left(\frac{\partial F^{n+1/4,k+1}}{\partial x} + \frac{\partial F^n}{\partial x}\right)$$
$$+ \frac{\sigma_a^{n+1/4,k}c}{2}\left(a(T^{n+1/4,k+1})^4 - E_r^{n+1/4,k+1}\right)$$
$$+ \frac{\sigma_a^n c}{2}\left(a(T^n)^4 - E_r^n\right) + \sigma_t^n\frac{u^n}{c}\left(\frac{4}{3}E_r^n u^n - F_r^n\right) , \tag{4.5a}$$

$$\frac{1}{3}\frac{\partial E_r^{n+1/4,k+1}}{\partial x} + \frac{1}{3}\frac{\partial E_r^n}{\partial x} + \frac{\sigma_t^{n+1/4,k}}{c}F^{n+1/4,k+1} + \frac{\sigma_t^n}{c}F^n =$$
$$\sigma_t^{n+1/4,k}\frac{4}{3}E^{n+1/4,k+1}\frac{u^n}{c} + \sigma_t^n\frac{4}{3}E^n\frac{u^n}{c} , \tag{4.5b}$$

$$\frac{4\left(E^{n+1/4,k+1} - E^*\right)}{\Delta t} = -\frac{\sigma_a^{n+1/4,k}c}{2}\left(a(T^{n+1/4,k+1})^4 - E_r^{n+1/4,k+1}\right)$$
$$- \frac{\sigma_a^n c}{2}\left(a(T^n)^4 - E_r^n\right) - \sigma_t^n\frac{u^n}{c}\left(\frac{4}{3}E_r^n u^n - F_r^n\right) . \tag{4.5c}$$

In order to solve these equations, we linearize the Planck function in Eq. (4.5a)

50

and Eq. (4.5c) and substitute the resulting expression for $T^{n+1/4,k+1}$ from Eq. (4.5c) into Eq. (4.5a). When $E_r^{n+1/4}$ and $F_r^{n+1/4}$ are computed, we update the material energy in the predictor implicitly with corrections for radiation momentum deposition and energy exchange. This process is repeated until $E_{M,i}^{n+1/4}$ and $E_{r,M,i}^{n+1/4}$ are converged.

To begin the corrector, we reconstruct the hydro variables, again, following the implicit update and use these, in conjunction with a Riemann solver, to compute the quarter-step cell-edge fluxes for the hydro variables, $F_{i+1/2}^{n+1/4}$. These fluxes allow us to compute a second-order approximation of the advection component of the rad-hydro system at $t^{n+1/2}$ using a Godunov update:

$$U_i^{**} = U_{M,i}^n + \frac{\Delta t}{2\Delta x} \left(F_{i-1/2}^{n+1/4} - F_{i+1/2}^{n+1/4} \right) . \tag{4.6}$$

Once this is computed, we update the fluid momentum in the corrector explicitly using the cell-averaged radiation momentum deposition at $t^{n+1/4}$.

$$
\begin{aligned}
\frac{2\rho_i^{n+1/2} \left(u_i^{n+1/2} - u_i^* \right)}{\Delta t} &= \frac{1}{2} \frac{\sigma_{t,L,i}^{n+1/4}}{c} \left(F_{r,L,i}^{n+1/4} - \frac{4}{3} E_{r,L,i}^{n+1/4} u_{L,i}^{n+1/4} \right) \\
&+ \frac{1}{2} \frac{\sigma_{t,R,i}^{n+1/4}}{c} \left(F_{r,R,i}^{n+1/4} - \frac{4}{3} E_{r,R,i}^{n+1/4} u_{R,i}^{n+1/4} \right) .
\end{aligned} \tag{4.7}
$$

Then, we solve the radiative transfer equations for the corrector step, computing the radiation energy density and radiation current and updating the material energy using the Crank-Nicholson method:

$$\frac{2\left(E_r^{n+1/2,k+1} - E_r^n\right)}{\Delta t} = -\frac{1}{2}\left(\frac{\partial F^{n+1/2,k+1}}{\partial x} + \frac{\partial F^n}{\partial x}\right) + \frac{\sigma_a^n c}{2}\left(a(T^n)^4 - E_r^n\right)$$

$$+ \frac{\sigma_a^{n+1/2,k} c}{2}\left(a(T^{n+1/2,k+1})^4 - E_r^{n+1/2,k+1}\right)$$

$$+ \sigma_t^{n+1/4}\frac{u^{n+1/4}}{c}\left(\frac{4}{3}E_r^{n+1/4}u^{n+1/4} - F_r^{n+1/4}\right), \qquad (4.8a)$$

$$\frac{1}{3}\frac{\partial E_r^{n+1/2,k+1}}{\partial x} + \frac{1}{3}\frac{\partial E_r^n}{\partial x} + \frac{\sigma_t^{n+1/2,k}}{c}F^{n+1/2,k+1} + \frac{\sigma_t^n}{c}F^n =$$

$$\sigma_t^{n+1/2,k}\frac{4}{3}E^{n+1/2,k+1}\frac{u^{n+1/4}}{c} + \sigma_t^n\frac{4}{3}E^n\frac{u^n}{c}, \qquad (4.8b)$$

$$\frac{2\left(E^{n+1/2,k+1} - E^{**}\right)}{\Delta t} = -\frac{\sigma_a^{n+1/2,k} c}{2}\left(a(T^{n+1/2,k+1})^4 - E_r^{n+1/2,k+1}\right)$$

$$- \frac{\sigma_a^n c}{2}\left(a(T^n)^4 - E_r^n\right)$$

$$- \sigma_t^{n+1/4}\frac{u^{n+1/4}}{c}\left(\frac{4}{3}E_r^{n+1/4}u^{n+1/4} - F_r^{n+1/4}\right). \qquad (4.8c)$$

Once $E_{M,i}^{n+1/2}$ and $E_{r,M,i}^{n+1/2}$ are converged, Cycle 1 is complete.

4.2   Cycle 2

In this section, we detail the second cycle of our radiation-hydrodynamics scheme. This cycle is very similar to the first cycle with the exception that we use a BDF2 step to solve for the radiation energy density and to update the material energy in the corrector. Like the first cycle, we begin by linearly reconstructing the hydro unknowns, $U_i^{n+1/2}$:

$$U_{L,i}^{n+1/2} = U_i^{n+1/2} - \frac{\Delta_i^{n+1/2}}{2}; \quad U_{R,i}^{n+1/2} = U_i^{n+1/2} + \frac{\Delta_i^{n+1/2}}{2}. \qquad (4.9)$$

Next, we evolve the hydro unknowns over another quarter time-step:

$$U_{M,i}^* = U_{M,i}^{n+1/2} + \frac{\Delta t}{4\Delta x}\left(F_{L,i}^{n+1/2} - F_{R,i}^{n+1/2}\right). \tag{4.10}$$

Again, note that $\rho_i^{n+3/4} = \rho_i^*$. We update the fluid momentum in the predictor of the second cycle:

$$
\begin{aligned}
\frac{4\rho_i^{n+3/4}\left(u_i^{n+3/4} - u_i^*\right)}{\Delta t} ={}& \frac{1}{2}\frac{\sigma_{t,L,i}^{n+1/2}}{c}\left(F_{r,L,i}^{n+1/2} - \frac{4}{3}E_{r,L,i}^{n+1/2}u_{L,i}^{n+1/2}\right) \\
&+ \frac{1}{2}\frac{\sigma_{t,R,i}^{n+1/2}}{c}\left(F_{r,R,i}^{n+1/2} - \frac{4}{3}E_{r,R,i}^{n+1/2}u_{R,i}^{n+1/2}\right).
\end{aligned}
\tag{4.11}
$$

Then, we enter our nonlinear iterations for the second-cycle predictor. As in the first-cycle predictor, in this loop we implicitly solve for the radiation energy density and current and update the material energy using the Crank-Nicholson method:

$$
\begin{aligned}
\frac{4\left(E_r^{n+3/4,k+1} - E_r^n\right)}{\Delta t} ={}& -\frac{1}{2}\left(\frac{\partial F^{n+3/4,k+1}}{\partial x} + \frac{\partial F^n}{\partial x}\right) \\
&+ \frac{\sigma_a^{n+3/4,k}c}{2}\left(a(T^{n+3/4,k+1})^4 - E_r^{n+3/4,k+1}\right) \\
&+ \frac{\sigma_a^{n+1/2}c}{2}\left(a(T^{n+1/2})^4 - E_r^{n+1/2}\right) \\
&+ \sigma_t^{n+1/2}\frac{u^{n+1/2}}{c}\left(\frac{4}{3}E_r^{n+1/2}u^{n+1/2} - F_r^{n+1/2}\right), \tag{4.12a}
\end{aligned}
$$

$$\frac{1}{3}\frac{\partial E_r^{n+3/4,k+1}}{\partial x} + \frac{1}{3}\frac{\partial E_r^{n+1/2}}{\partial x} + \frac{\sigma_t^{n+3/4,k}}{c}F^{n+3/4,k+1} + \frac{\sigma_t^{n+1/2}}{c}F^{n+1/2} =$$

$$\sigma_t^{n+3/4,k}\frac{4}{3}E^{n+3/4,k+1}\frac{u^{n+1/2}}{c} + \sigma_t^{n+1/2}\frac{4}{3}E^{n+1/2}\frac{u^{n+1/2}}{c},$$

$$(4.12\text{b})$$

$$\frac{4\left(E^{n+3/4,k+1}-E^*\right)}{\Delta t} = -\frac{\sigma_a^{n+3/4,k}c}{2}\left(a(T^{n+3/4,k+1})^4 - E_r^{n+3/4,k+1}\right)$$

$$-\frac{\sigma_a^{n+1/2}c}{2}\left(a(T^{n+1/2})^4 - E_r^{n+1/2}\right)$$

$$-\sigma_t^{n+1/2}\frac{u^{n+1/2}}{c}\left(\frac{4}{3}E_r^{n+1/2}u^{n+1/2} - F_r^{n+1/2}\right). \qquad (4.13)$$

Then, Eq. (4.12) and Eq. (4.13) are repeated until $E_{M,i}^{n+3/4}$ and $E_{r,M,i}^{n+3/4}$ are converged. To begin the cycle 2 corrector, we reconstruct the hydro variables, again, following the implicit update and use these, in conjunction with a Riemann solver, to compute the three quarter-step cell-edge fluxes for the hydro variables, $F_{i+1/2}^{n+3/4}$. Using these fluxes, we compute the advection component of the rad-hydro system at t^{n+1} using a Godunov update:

$$U_i^{**} = U_{M,i}^{n+1/2} + \frac{\Delta t}{2\Delta x}\left(F_{i-1/2}^{n+3/4} - F_{i+1/2}^{n+3/4}\right). \qquad (4.14)$$

Computing this, we update the fluid momentum in the corrector explicitly using radiation values at $t^{n+3/4}$.

$$\frac{\rho_i^{n+1}\left(u_i^{n+1} - u_i^{**}\right)}{\Delta t} = \frac{\sigma_{t,i}^{n+1/2}}{c}\left(F_{r,i}^{n+1/2} - \frac{4}{3}E_{r,i}^{n+1/2}u_i^{n+1/2}\right). \qquad (4.15)$$

Finally, we enter the nonlinear iterations for the corrector step of Cycle 2. Here,

we implicitly solving for the radiation energy density and current using the BDF2 method:

$$\frac{\left(E_r^{n+1,k+1} - E_r^n\right)}{\Delta t} = -\frac{1}{3}\left(\frac{\partial F^{n+1,k+1}}{\partial x} + \frac{\partial F^{n+1/2}}{\partial x} + \frac{\partial F^n}{\partial x}\right)$$
$$+ \frac{\sigma_a^{n+1,k}c}{3}\left(a(T^{n+1,k+1})^4 - E_r^{n+1,k+1}\right)$$
$$+ \frac{\sigma_a^{n+1/2}c}{3}\left(a(T^{n+1/2})^4 - E_r^{n+1/2}\right) + \frac{\sigma_a^n c}{3}\left(a(T^n)^4 - E_r^n\right)$$
$$+ \sigma_t^{n+1/2}\frac{u^{n+1/2}}{c}\left(\frac{4}{3}E_r^{n+1/2}u^{n+1/2} - F_r^{n+1/2}\right) , \qquad (4.16a)$$

$$\frac{1}{3}\frac{\partial E_r^{n+1,k+1}}{\partial x} + \frac{1}{3}\frac{\partial E_r^{n+1/2}}{\partial x} + \frac{1}{3}\frac{\partial E_r^n}{\partial x} + \frac{\sigma_t^{n+1,k}}{c}F^{n+1,k+1} + \frac{\sigma_t^{n+1/2}}{c}F^{n+1/2} + \frac{\sigma_t^n}{c}F^n =$$
$$\sigma_t^{n+1,k}\frac{4}{3}E^{n+1,k+1}\frac{u^{n+1/2}}{c} + \sigma_t^{n+1/2}\frac{4}{3}E^{n+1/2}\frac{u^{n+1/2}}{c} + \sigma_t^n\frac{4}{3}E^n\frac{u^{n+1/2}}{c} ,$$
$$(4.16b)$$

Using these values, we compute the full-step material energy. Because this is a full-step calculation, instead of updating the values computed in Eq. (4.14), we treat the hydrodynamic fluxes, $F^{n+1/4}$ and $F^{n+3/4}$, from the first and second cycles as sources for the BDF2 equation.

$$\frac{\left(E^{n+1,k+1} - E^n\right)}{\Delta t} = -\frac{\sigma_a^{n+1,k}c}{3}\left(a(T^{n+1,k+1})^4 - E_r^{n+1,k+1}\right)$$
$$- \frac{\sigma_a^{n+1/2}c}{3}\left(a(T^{n+1/2})^4 - E_r^{n+1/2}\right) - \frac{\sigma_a^n c}{3}\left(a(T^n)^4 - E_r^n\right)$$
$$- \sigma_t^{n+1/2}\frac{u^{n+1/2}}{c}\left(\frac{4}{3}E_r^{n+1/2}u^{n+1/2} - F_r^{n+1/2}\right)$$
$$- \frac{1}{2}\left(\frac{\partial F^{n+1/4}}{\partial x} + \frac{\partial F^{n+3/4}}{\partial x}\right) . \qquad (4.17)$$

We iterate Eq. (4.16) and Eq. (4.17) until $E_{M,i}^{n+1}$ and $E_{r,M,i}^{n+1}$ are converged, and the solution over the full time step is complete.

5. MANUFACTURED SOLUTIONS

Order-accuracy is a concept in numerical methods that describes the rate at which the computed solution from a method converges to the exact solution of the model equations as the mesh spacing decreases. To understand this, we must first define the truncation error of a method. Truncation error arises when one uses a finite process to approximate the solution to an infinite, or continuous, system. In this case, because our method uses finite difference and finite element approximations to estimate the solution to our continuously varying radiation hydrodynamics model, we will have truncation error due to discretization error.

The term "truncation error" stems from the fact that, if we were to expand the solution to the continuous system using an infinite series, the expansion from a finite approximation to that continuous system would be exact to a certain number of terms in that series. Thus, the finite solution is exact to a truncated number of terms in the series expansion, and the terms in which they differ represent the truncation error in the approximation. If one represents the continuous and finite solutions using a Taylor series, each term in that series is associated with the mesh spacing raised to a power, e.g. Δx^p. If the finite solution expansion is accurate through the Δx^{p-1} term, the method is said to be p-th order accurate, since the leading term in the truncation error as Δx approaches 0 will be the Δx^p term.

To determine order-accuracy, we need a way to compute the truncation error of our method. This can be challenging, as it requires a problem set to which the exact solution may be obtained or very closely estimated. One approach is to prescribe geometric, boundary, and initial conditions in such a way that an analytical solution to the system may be found directly. However, due to the complexity of

our radiation hydrodynamics model, solutions that can be obtained in this manner would likely be too simple, without sufficient variation in space and time, to be useful in demonstrating order-accuracy. Instead, we use the Method of Manufactured Solutions (MMS). With MMS, we assume a functional form of the exact solution and use that to derive a set of forcing functions that can be used to reproduce those solutions with our numerical method. This allows us to prescribe an exact solution with sufficient variation in space and time to fully test the coupling between the radiation and hydrodynamics while ensuring that the solution space is continuous.

For these tests, we use the manufactured solutions developed by McClarren and Lowrie in [22] as a foundation. These solutions are composed of a combination of trigonometric functions with periodic boundary conditions. Our manufactured sources are a modification of those in [22], which uses a P_1 radiation model. Our modifications primarily include eliminating the time derivative of F_r for the diffusion approximation and the use of the simplified material motion model developed by Morel described in Section 2. As in [22], we consider both an equilibrium diffusion limit and a streaming limit solution.

To this point, we have considered the dimensionalized form of our rad-hydro system. However, to derive the sources for the manufactured solutions, we consider a non-dimensionalized form of this system, as presented in [22]. To non-dimensionalize our system, we first define a set of characteristic dimensional parameters:

$\hat{L}$ (reference length)

$\hat{\rho}_0$ (reference material mass density)

$\hat{T}_0$ (reference material temperature)

$\hat{a}_0$ (reference material sound speed)

$\hat{c}$ (speed of light)

$\hat{\alpha}_r$ (radiation constant)

Then, we define a set of non-dimensional quantities in terms of their dimensional counterparts and the characteristic dimensional parameters:

$x = \frac{\hat{x}}{\hat{L}}$ (spatial coordinate)

$t = \frac{\hat{t}\hat{a}_0}{\hat{L}}$ (time coordinate)

$\rho = \frac{\hat{\rho}}{\hat{\rho}_0}$ (material density)

$v = \frac{\hat{v}}{\hat{a}_0}$ (material velocity)

$e = \frac{\hat{e}}{\hat{a}_0^2}$ (internal specific energy)

$p = \frac{\hat{p}}{\hat{\rho}\hat{a}_0^2}$ (material pressure)

$T = \frac{\hat{T}}{\hat{T}_0}$ (material temperature)

$\Theta = \frac{\hat{\Theta}}{\hat{T}_0}$ (radiation temperature)

$\sigma_a = \frac{\hat{\sigma}_a\hat{L}\hat{c}}{\hat{a}_0}$ (absorption cross-section)

$\sigma_t = \frac{\hat{\sigma}_t\hat{L}\hat{c}}{\hat{a}_0}$ (total cross-section)

Substituting these into (2.1) and adding general source terms, we obtain a non-dimensionalized form of our RH system:

$$\frac{\partial \rho}{\partial t} + \frac{\partial}{\partial x}\left(\rho u\right) = Q_\rho\,, \tag{5.1a}$$

59

$$\frac{\partial (\rho u)}{\partial t} + \frac{\partial}{\partial x} \left(\rho u^2 + p \right) = -\mathbb{P} S_F + Q_v \,, \tag{5.1b}$$

$$\frac{\partial E}{\partial t} + \frac{\partial}{\partial x} \left[(E + p) \, u \right] = -\mathbb{P}\mathbb{C} S_E + Q_E \,, \tag{5.1c}$$

$$\frac{\partial E_r}{\partial t} + \frac{\partial \mathbb{C} F_r}{\partial x} = S_E + Q_{E_r} \,, \tag{5.1d}$$

$$\frac{\mathbb{C}}{3} \frac{\partial E_r}{\partial x} = \mathbb{C} S_F \,, \tag{5.1e}$$

Here, we have defined a set of non-dimensionalized parameters $\mathbb{C}$ and $\mathbb{P}$, where

$$\mathbb{P} = \frac{\alpha_r T_0^4}{\rho_0 a_0^2} \,, \mathbb{C} = \frac{c}{a_0} \,. \tag{5.2}$$

Thus, $\mathbb{C}$ is the ratio of the speed of light to the characteristic speed of sound of the material, and $\mathbb{P}$ is proportional to the ratio of the characteristic radiant energy of the material to the characteristic kinetic energy of the material. Note, also, that (5.1e) doesn't include a source term. This is due to the fact that the variation of the radiative flux is defined explicitly by the other unknowns. In addition to our non-dimensionalized parameters, we define the following:

$$S_E = \mathbb{C} \sigma_a \left(T^4 - E_r \right) + \sigma_t v F_{r,0} \,, \tag{5.3a}$$

$$S_F = -\sigma_t F_{r,0} \,, \tag{5.3b}$$

$$F_{r,0} = F_r - \frac{4}{3} \frac{v}{\mathbb{C}} E_r \,. \tag{5.3c}$$

5.1   Diffusion Solution

We begin by examining the manufactured solution for a diffusive regime. This represents a problem in which absorption and re-emission of radiation dominates streaming, and the radiation energy is in local equilibrium with the material tem-

perature. Numerically, this represents a case in which the opacity is large, and the radiation mean-free path is not resolved by the cell spacing. Characterizing this solution using asymptotic analysis, the leading order solution for the radiation energy density [19] is given by:

$$E_r = T^4 \,. \tag{5.4a}$$

We set the non-dimensionalized, functional form of the exact hydrodynamics solution to be:

$$\rho = \sin(x - t) + 2 \,, \tag{5.5a}$$

$$v = \cos(x - t) + 2 \,, \tag{5.5b}$$

$$p = \alpha \left(\cos(x - t) + 2 \right) \,. \tag{5.5c}$$

Using the equation of state, the exact material temperature is:

$$T = \frac{\alpha\gamma \left(\cos(x - t) + 2 \right)}{\sin(x - t) + 2} \,, \tag{5.6}$$

Now, substituting (5.6) into (5.4) and (5.1e), we have the functional form of the radiation energy density and flux:

$$E_r = \frac{\alpha^4 \gamma^4 \left(\cos(x - t) + 2 \right)^4}{\left(\sin(x - t) + 2 \right)^4} \,, \tag{5.7a}$$

$$F_r = \frac{4\alpha^4 \gamma^4 \left(\cos(x - t) + 2 \right)^5}{3\mathbb{C} \left(2 - \sin t - x \right)^4} - \frac{4\alpha^4 \gamma^4 \left(\cos(x - t) + 2 \right)^3 \sin t - x}{3\sigma \left(2 - \sin(t - x) \right)^4}$$
$$- \frac{4\alpha^4 \gamma^4 \cos(x - t) \left(\cos(x - t) + 2 \right)^4}{3\sigma \left(2 - \sin(t - x) \right)^5} \,. \tag{5.7b}$$

61

The material unknowns given by (5.5) and (5.6) are shown in Figure 5.1, and the radiation energy density is shown in Figures 5.2. Substituting (5.5), (5.6), and (5.7) into (5.1), we solve for the forcing functions necessary to reproduce those solutions. These functions are as follows:

$$Q_\rho = 2\sin(t-x) + \cos(t-x) + \cos(2(t-x)),\tag{5.8a}$$

$$Q_v = \frac{4\alpha^4\gamma^4 \mathrm{PP}(\cos(t-x)+2)^3(-2\sin(t-x)+2\cos(t-x)+1)}{3(\sin(t-x)-2)^5}$$

$$+ \alpha\sin(t-x) + (\sin(t-x)-2)\sin(t-x) + \cos(t-x)(\cos(t-x)+2)^2$$

$$- \cos(t-x)(\cos(t-x)+2) - 2(\sin(t-x)-2)\sin(t-x)(\cos(t-x)+2),$$

$$\tag{5.8b}$$

$$Q_E = -\frac{4\alpha^4\gamma^4 \mathrm{PP}(\cos(t-x)+2)^4(-2\sin(t-x)+2\cos(t-x)+1)}{3(\sin(t-x)-2)^5}$$

$$- \frac{1}{2}\cos(t-x)(\cos(t-x)+2)\left(-\frac{2\alpha}{(\gamma-1)(\sin(t-x)-2)} + \cos(t-x)+2\right)$$

$$+ \frac{1}{2}\sin(t-x)(\cos(t-x)+2)\bigg(2\alpha$$

$$+ (2-\sin(t-x))\left(-\frac{2\alpha}{(\gamma-1)(\sin(t-x)-2)} + \cos(t-x)+2\right)\bigg)$$

$$+ \frac{1}{8(\gamma-1)}(\cos(t-x)+2)\Big(8\left(\sin(t-x)((\alpha+4)\gamma+2(\gamma-1)\cos(t-x)-4\right)$$

$$+2(\gamma-1)\cos(2(t-x))) + 17(\gamma-1)\cos(t-x)+3(\gamma-1)\cos(3(t-x))\Big)$$

$$+ (2-\sin(t-x))\bigg(\frac{\alpha\sin(t-x)}{(\gamma-1)(\sin(t-x)-2)}$$

$$+ \frac{\alpha\cos(t-x)(\cos(t-x)+2)}{(\gamma-1)(\sin(t-x)-2)^2} - \sin(t-x)(\cos(t-x)+2)\bigg),\tag{5.8c}$$

62

$$Q_{ER} = \frac{1}{12\sigma\left(\sin(t-x)-2\right)^6}\Big(\alpha^4\gamma^4(\cos(t-x)+2)^2(-8(23\mathbb{C}+235\sigma)\cos(t-x)$$

$$-16(\mathbb{C}+17\sigma)\cos(2(t-x))+328\mathbb{C}\sin(t-x)+256\mathbb{C}\sin(2(t-x))$$

$$+8\mathbb{C}\sin(3(t-x))-8\mathbb{C}\cos(3(t-x))-320\mathbb{C}-1452\sigma+1678\sigma\sin(t-x)$$

$$+1088\sigma\sin(2(t-x))+237\sigma\sin(3(t-x))+12\sigma\sin(4(t-x))$$

$$-\sigma\sin(5(t-x))+120\sigma\cos(3(t-x))+28\sigma\cos(4(t-x)))\Big). \qquad (5.8\text{d})$$
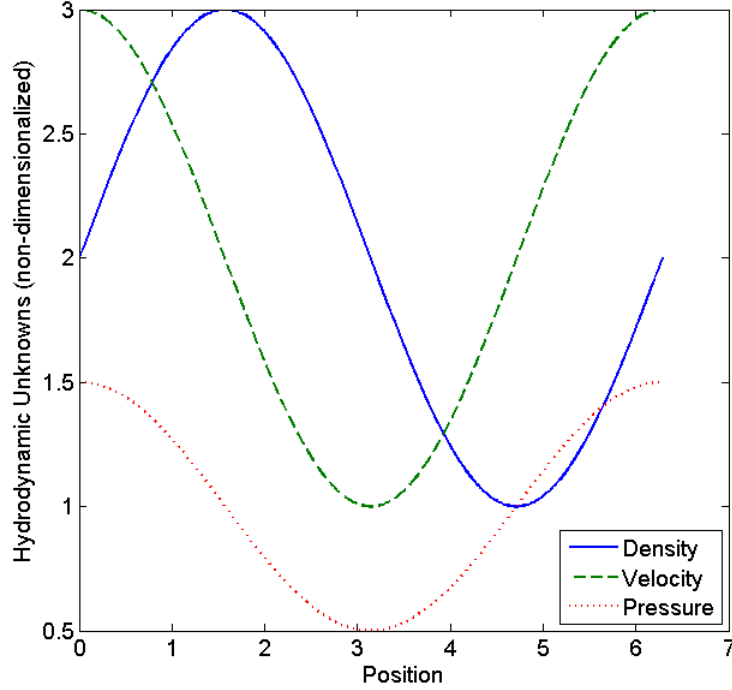

Figure 5.1: Exact solution for the hydrodynamic unknowns, ρ, u, and p, for the equilibrium diffusion limit at $t = 0$.

Analytically, using (5.8) as a source for (5.1) yields the exact solution given by (5.5), (5.6), and (5.7). Thus, we can use these functions as a framework for testing
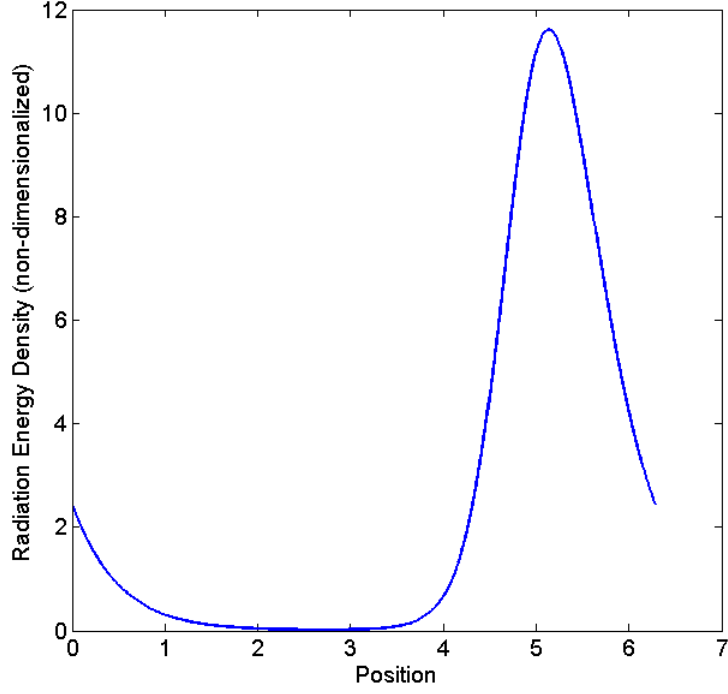
Figure 5.2: Exact solution for the radiation energy density, E_r, for the equilibrium diffusion limit at $t = 0$.

the accuracy of our RH algorithm in both time and space. However, because our method is defined using the dimensionalized RH system, we must re-dimensionalize (5.8) to use these sources. We do this as follows:

$$\hat{Q}_\rho = \frac{\hat{\rho}_0 \hat{a}_0}{\hat{L}} Q_\rho \,, \tag{5.9a}$$

$$\hat{Q}_u = \frac{\hat{\rho}_0 \hat{a}_0{}^2}{\hat{L}} Q_u \,, \tag{5.9b}$$

$$\hat{Q}_E = \frac{\hat{\rho}_0 \hat{a}_0{}^3}{\hat{L}} Q_E \,, \tag{5.9c}$$

$$\hat{Q}_{E_r} = \frac{\alpha_r \hat{T}_0{}^4 \hat{a}_0}{\hat{L}} Q_{E_r} \,. \tag{5.9d}$$

64

This manufactured solution affords us the opportunity to test the behavior of our method in the equilibrium diffusion limit. To test this limit, we examine the error of the solution as the mesh is refined while preserving the optical thickness, τ, of each cell. The error of a method that preserves the equilibrium diffusion limit will decrease as the mesh is refined for a fixed τ and CFL condition; however, a method that does not have this limit will only converge to the correct solution if τ decreases with the mesh spacing. In order to test the thick diffusion limit, it is necessary to set $\tau \gg 1$. For our test problems, we set $\tau = 100\pi$, $\alpha = 0.5$, $\gamma = 5/3$, and $\mathbb{P} = 0.001$. To keep τ constant as we vary the mesh spacing, we define a parameter ϵ and vary Δx, $\mathbb{C}$, and σ with ϵ as follows:

$$\Delta x = \frac{\pi}{10}\epsilon \, , \tag{5.10a}$$

$$\mathbb{C} = \sigma = \frac{1000}{\epsilon} \, . \tag{5.10b}$$

Thus, as ϵ approaches zero, Δx also approaches zero, $\mathbb{C}$ and σ become very large, and τ remains constant. The time step is bound by the Courant limit:

$$CFL = \frac{\mathbb{C}\Delta t}{\Delta x} \, . \tag{5.11}$$

By fixing CFL, Eq. (5.10) requires that Δt decreases according to ϵ^2. To meet the CFL condition, $CFL = 0.3$, we use fixed timesteps and set Δt as:

$$\Delta t = \frac{t_{fin}}{2000}\epsilon^2 \, . \tag{5.12}$$

Substituting these values into (5.2) and using the relation $T_0 = \alpha_0^2$, we obtain the characteristic variables, ρ_0, α_0, and T_0. The slab thickness is 2π cm, and the final time, t_{fin}, is 0.105 shakes.

We compute the spatially-distributed error in the computational solution by subtracting the solution computed at the final time from the exact solution at that time. Then, we take the L_2 norm of the spatially distributed error to get a measure of the total error of the final solution. Figures 5.3, 5.4, and 5.5 show the errors in the material velocity, material temperature, and radiation energy density, respectively, between the computed and exact solution for the equilibrium diffusion limit as the spatial and temporal mesh is refined. In each of these figures, we see that, as the mesh is refined, the error varies with second-order accuracy.
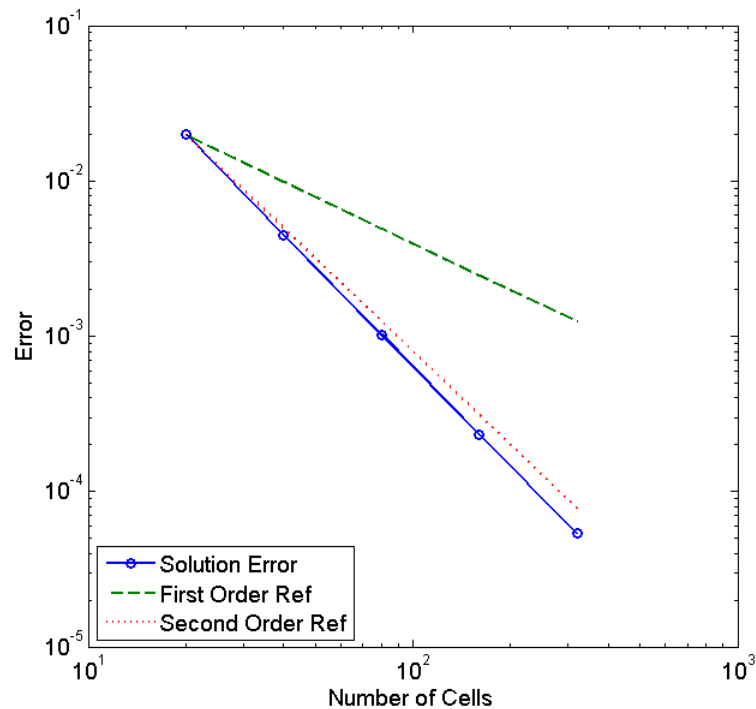

Figure 5.3: Error in the material velocity between the computed and exact solution for the diffusive limit manufactured solution.
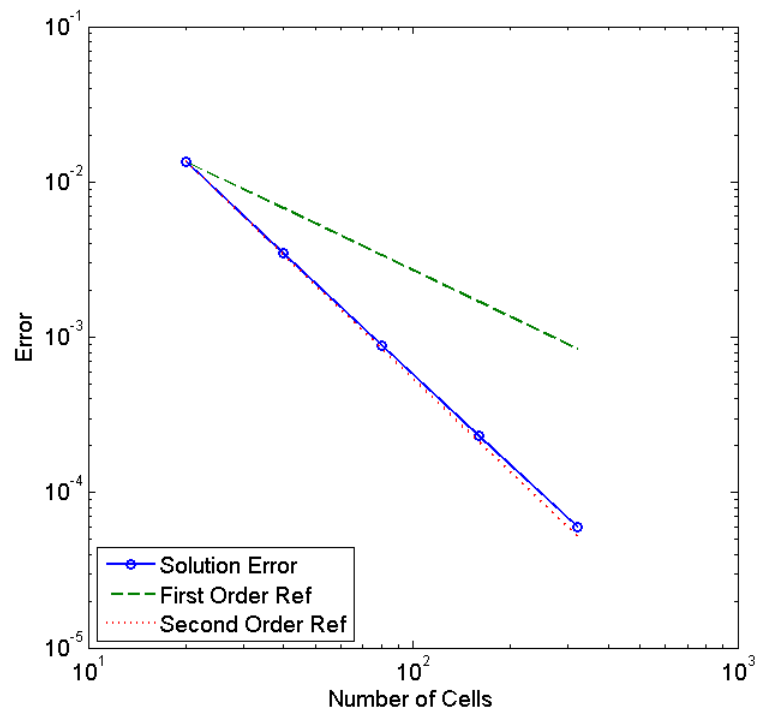
Figure 5.4: Error in the material temperature between the computed and exact solution for the diffusive limit manufactured solution.
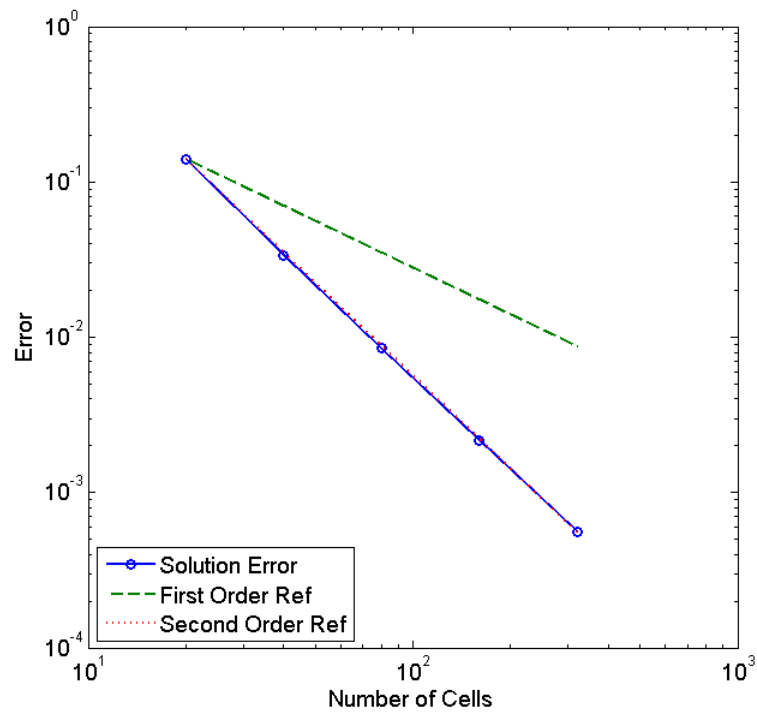
Figure 5.5: Error in the radiation energy density between the computed and exact solution for the diffusive limit manufactured solution.

5.2   Streaming Limit

Next, we consider the manufactured solution for the streaming limit. In this limit, radiation streaming dominates a relatively small radiation absorption/re-emission term. Here, we keep the re-emission term small by making the opacity relatively small so that the radiation is nearly transparent to the material. Therefore, in contrast to the equilibrium diffusion limit which represents very tight coupling between the radiation and hydrodynamic components, this limit represents very weak coupling between the two. Also, because the radiation streams much faster than the material, this results in a solution in which the unknowns evolve at significantly different time scales. The functional form of the exact streaming solution is given by:

$$\rho = \sin\left(x - t\right) + 2\,, \tag{5.13a}$$

$$v = \frac{1}{\sin\left(x - t\right) + 2}\,, \tag{5.13b}$$

$$p = \alpha\left(\cos\left(x - t\right) + 2\right)\,, \tag{5.13c}$$

$$E_r = \alpha\left(\sin\left(x - \mathbb{C}t\right) + 2\right)\,. \tag{5.13d}$$

Here, was can see that the wave speed of the radiation energy density is faster than that of the hydrodynamic unknowns by a factor of $\mathbb{C}$. The exact solution for the streaming solution hydrodynamic unknowns are shown in Figure 5.6, and the radiation energy density is shown in Figure 5.7.

This solution is also defined to mimic an isothermal flow regime, in which the radiation varies rapidly enough that changes in the material temperature are suppressed. In this case, the exact solution for the material temperature is a constant given by:
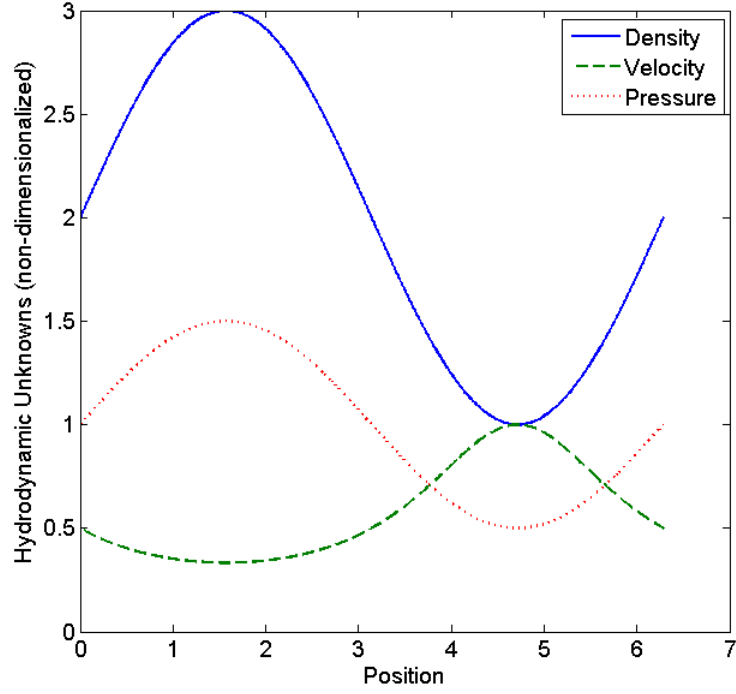
$$T = \alpha\gamma\,. \tag{5.14}$$

Figure 5.6: Exact solution for the hydrodynamic unknowns, ρ, u, and p, for the streaming limit at $t = 0$.

Again, we derive the forcing functions corresponding to these solutions by substituting (5.13) and (5.14) into (5.1). The resulting functions are as follows:

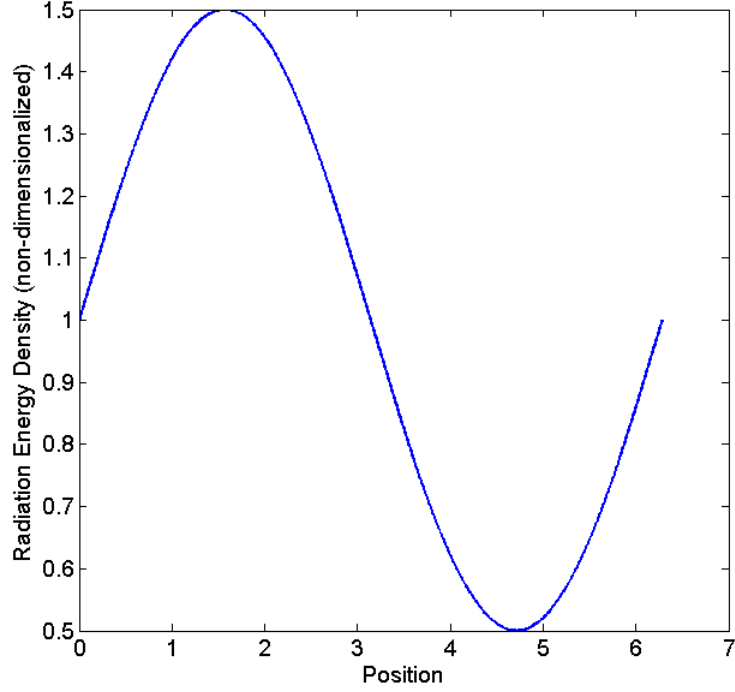$$Q_\rho = -\cos(t - x)\,, \tag{5.15a}$$

70

Figure 5.7: Exact solution for the radiation energy density, E_r, for the streaming limit at $t = 0$.

$$Q_v = \frac{1}{3}\alpha\mathbb{P}\cos(\mathbb{C}t - x) + \cos(t - x)\left(\alpha - \frac{1}{(\sin(t - x) - 2)^2}\right), \qquad (5.15\text{b})$$

$$Q_E = \frac{1}{3}\alpha\mathbb{P}\left(3\mathbb{C}\sigma\left(\alpha^3\gamma^4 + \sin(\mathbb{C}t - x) - 2\right) + \frac{\cos(\mathbb{C}t - x)}{\sin(t - x) - 2}\right)$$

$$+ \frac{1}{4(\gamma - 1)(\sin(t - x) - 2)^3}\left(\cos(t - x)((-51\alpha + 2\gamma - 2)\sin(t - x)\right.$$

$$\left. + \alpha(\sin(3(t - x)) + 44) - 12\alpha\cos(2(t - x)))\right), \qquad (5.15\text{c})$$

71

$$Q_{ER} = \frac{1}{3}\alpha\left(-3\alpha^3\gamma^4\mathbb{C}\sigma + 6\mathbb{C}\sigma - 3\mathbb{C}\sigma\sin(\mathbb{C}t - x) - \frac{\mathbb{C}\sin(\mathbb{C}t - x)}{\sigma}\right.$$
$$\left. + \left(-3\mathbb{C} - \frac{5}{\sin(t - x) - 2}\right)\cos(\mathbb{C}t - x) + \frac{4\cos(t - x)(\sin(\mathbb{C}t - x) - 2)}{(\sin(t - x) - 2)^2}\right).$$

$$(5.15\text{d})$$

For this test, we set $\alpha = 0.5$, $\gamma = 5/3$, $\mathbb{C} = 10$, and $\sigma = 1$. The slab thickness is 2π cm, and the final time is 0.011 shakes. As with the equilibrium diffusion limit test, we approximate the exact solution given by (5.13) and (5.14) computationally by using (5.15) as sources for our method, redimensionalizing these sources using (5.9). We compute the L_2 norm of the spatially-distributed error as outlined for the equilibrium diffusion limit test for various mesh refinements, in which $\Delta x/\Delta t$ is kept constant. Figures 5.8, 5.9, and 5.10 compare the error in the material velocity, material temperature, and radiation energy density, respectively, with reference lines to first and second-order accuracy. Again, for this test, we see that, as the mesh is refined, the method shows second-order accuracy.

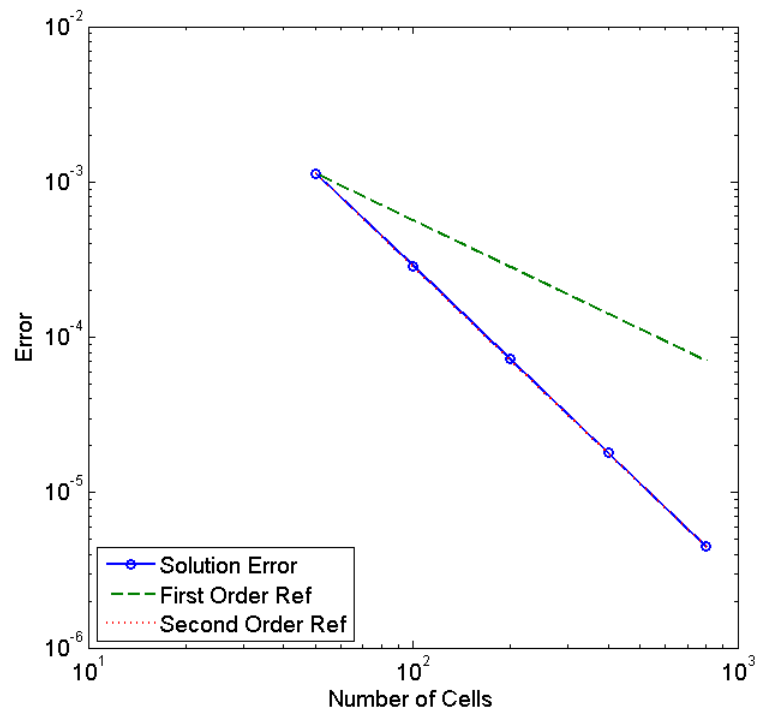Figure 5.8: Error in the material velocity between the computed and exact solution for the streaming limit manufactured solution.
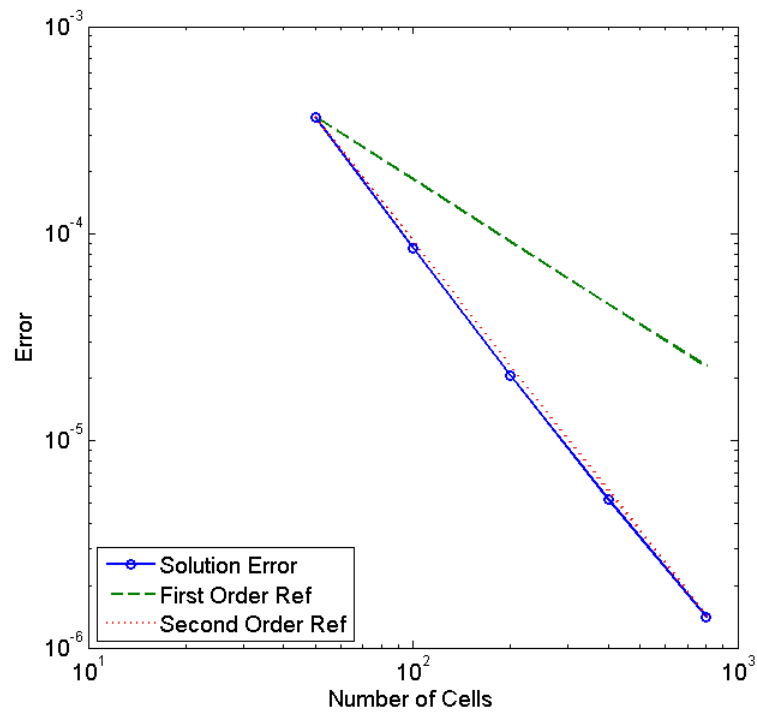
Figure 5.9: Error in the material temperature between the computed and exact solution for the streaming limit manufactured solution.
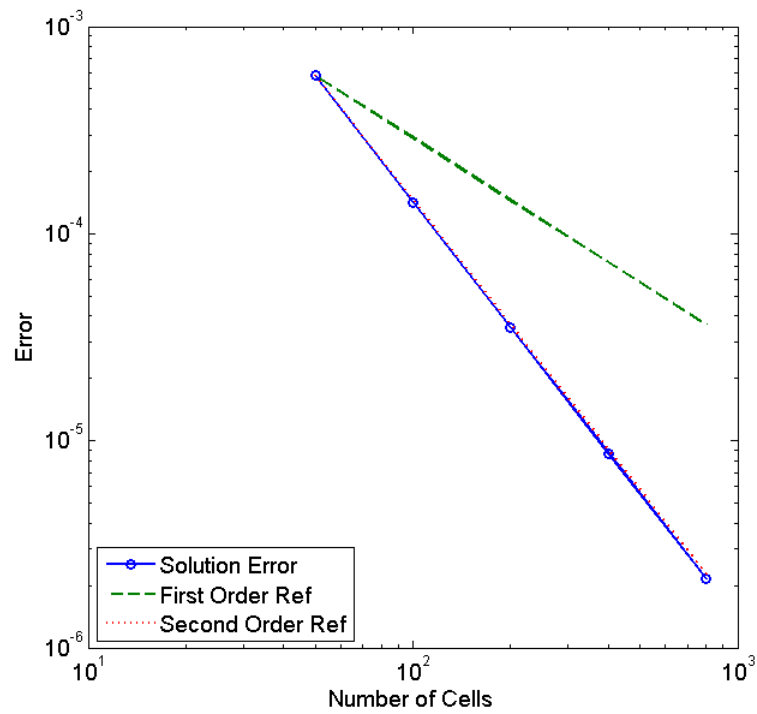
Figure 5.10: Error in the radiation energy density between the computed and exact solution for the streaming limit manufactured solution.

6. RADIATIVE SHOCKS

6.1 Structure of Radiative Shocks

A shock wave is a disturbance propagating through a medium and characterized by rapid or, in some cases, nearly discontinuous changes in the properties of that medium. Hydrodynamic shocks often correspond to a very sharp decrease in fluid velocity and a corresponding increase in density, pressure, and temperature due to compression across the shock front. Neglecting viscosity in a pure hydrodynamic regime, all variables are discontinuous at the shock front. A radiative shock is a shock wave moving through a fluid with sufficient speed or internal energy that the radiation energy and/or pressure plays a significant role in the dynamics. Even neglecting viscosity, the radiation intensity is never discontinuous in a radiative shock, and the hydrodynamic variables may or may not be discontinuous. Radiative shocks occur, for example, in astrophysical systems such as shocks within stars or shocks formed when active galactic nuclei capture stars. They have also been generated in laboratory experiments in which Be is shocked via laser irradiation through xenon gas [27].

The widely used books by Zel'dovich and Raizer [35] and Mihalas and Mihalas [23] provide the classic descriptions of radiative shocks. The structure of optically thick radiative shocks, which we consider here, has been described in more detail by Drake in [6] and by Lowrie and Edwards in [17]. These are shocks in which the medium appears infinite to photons entering or leaving the shock. Thus, in a 1-D infinite medium slab geometry, radiative shocks are always optically thick so long as the opacity is never zero.

There are three key regions of radiative shocks - a precursor region, a hydrody-

namic shock, and a relaxation region. As demonstrated in [17], not every radiative shock will exhibit each of these features. Instead, the character of a given shock depends upon several dimensionless parameters: the shock Mach number, the ratio of the radiant energy to the kinetic energy of the material $\mathbb{P}$, the radiative diffusivity κ, which is defined later, and the non-dimensional absorption cross-section σ_a. Fig. 6.1 illustrates the important features of a radiative shock, which we describe here in further detail.
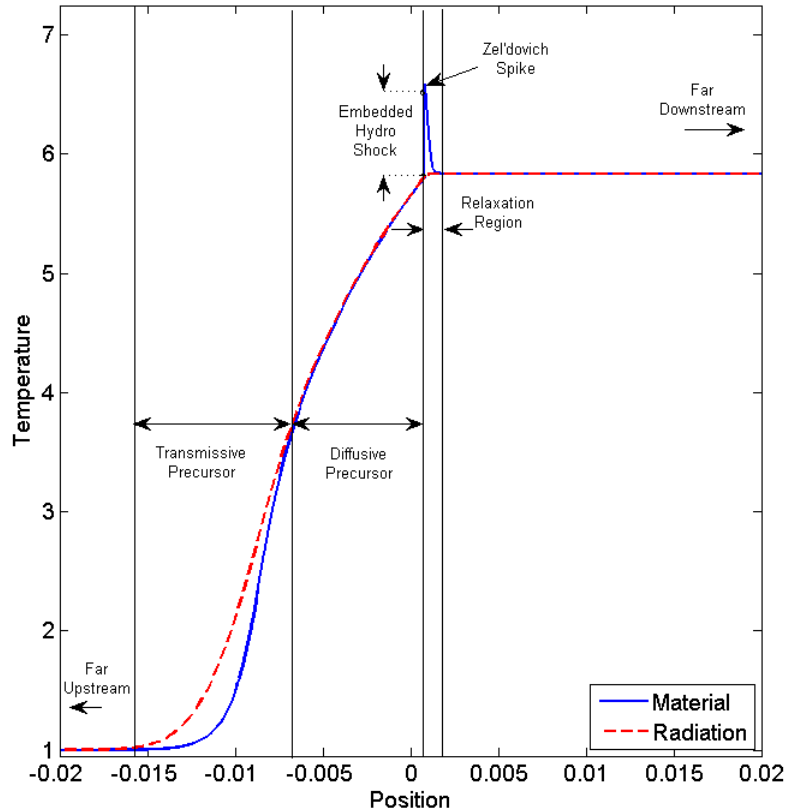

Figure 6.1: Illustration of the important features in the material and radiation temperature profiles for an example radiative shock.

Similar to standard hydrodynamic shocks, far upstream of radiative shocks, there is a steady flow of incoming fluid with a corresponding steady net radiation energy flux. As the material moves downstream, the first feature of the radiative shock it encounters is the precursor region. This region is created by the relatively high radiation energy flux moving upstream from the compressed, heated material in the hydrodynamic shock. Drake further differentiates this region into a "transmissive" precursor and a "diffusive" precursor. In this description, the transmissive precursor is distinguished by an exponential rise in temperature as a result of heating from the decaying radiation energy field. Nearer to the hydrodynamic shock as the radiation flux intensifies, the shape of the diffusive precursor becomes similar to that of a Marshak wave, discussed in [23], in which material is heated from a constant-temperature radiation source at the boundary.

After the precursor region, the fluid encounters the embedded hydrodynamic shock. Here, the fluid undergoes the same compressive effects as in a standard hydrodynamic shock with the exception that the initial jump conditions correspond to the precursor values rather than the far-upstream values. Because this jump occurs on the scale of a few ion-ion mean-free-paths, which is very much smaller than typical mesh spacing for problems of interest, it is entirely reasonable to treat this shock as a discontinuity [6]. For a steady shock, identifying the precursor state with the subscript "p" and the shocked state with the subscript "s", the discontinuity may be computed using the Rankine-Hugoniot relationship, which establishes the continuity of the hydrodynamic flux across the shock [17]:

$$(\rho v)_p = (\rho v)_s \; , \tag{6.1a}$$

$$\left(\rho v^2 + p\right)_p = \left(\rho v^2 + p\right)_s \; , \tag{6.1b}$$

$$[(\rho E + p)\, v]_p = [(\rho E + p)\, v]_s \; . \tag{6.1c}$$

Following the hydrodynamic shock, the fluid enters the relaxation (or cooling) region. In shocks with an isothermal sonic point (ISP), the post-shock temperature may significantly exceed the far-downstream fluid temperature. This phenomenon, called a Zel'dovich spike, is caused by the compression from the hydrodynamic shock combined with radiative effects which can serve to increase those compressive effects. The Zel'dovich spike is described in greater detail in [35, 17]. The effect of this dramatic increase in temperature is to drive the fluid far out of equilibrium with the radiation. As the material cools, the relaxation region extends downstream from the hydrodynamic shock until the radiation and material temperatures have equilibrated and the fluid is, again, steady.

As described in [6], the distinct features of radiative shocks stem from large differences in important spatial scales. The radiation emission and absorption occurs over the largest spatial scale, which gives rise to the precursor region upstream of the hydrodynamic shock and the cooling down region downstream of the hydrodynamic shock. The hydrodynamic shock, itself, occurs on the viscous scale, which is the smallest spatial scale of interest. Lowrie and Edwards quantify the range of shocks over which hydrodynamic shocks and isothermal sonic points may be present [17]. They, also, show that, in the case of no hydrodynamic shock, the solution will be continuous in all variables, and that, when an isothermal sonic point is present, the maximum temperature of the shock will exceed the far-downstream temperature.

6.2   Simulation of Radiative Shocks

Reproducing radiative shocks accurately, particularly in the optically thick regime, represents a challenging problem in the simulation of radiation hydrodynamics. However, because many problems of interest include radiative shocks, it is imperative that

a numerical scheme be able to meet these challenges well. In the remainder of this section, we demonstrate the capability of our rad-hydro algorithm to compute accurate radiative shock solutions by reproducing the semi-analytic shocks detailed in [17]. First, we describe our procedure to generate the shocks and, then, compare our computational results with the semi-analytic solutions.

We begin by computing the far-downstream fluid state associated with a prescribed set of far-upstream conditions. As we previously mentioned, these far-upstream conditions, and subsequently, the radiative shock itself, are specified by the shock Mach number M, the parameters $\mathbb{P}$ and σ_a, and the radiative diffusivity κ, which is given by:

$$\kappa = \frac{\hat{c}}{3\hat{\sigma}_t \hat{a}_0 \hat{L}} \ .$$

(6.2)

The equations that describe the overall jump from the upstream to the downstream states are a modified version of the Rankine-Hugoniot conditions derived by equating the flux terms from the fluid conservation equations in the rad-hydro model. These modified Rakine-Hugoniot conditions are given-by:

$$(\rho v)_0 = (\rho v)_1 \ ,$$

(6.3a)

$$\left(\rho v^2 + p^*\right)_0 = \left(\rho v^2 + p^*\right)_1 \ ,$$

(6.3b)

$$\left[\left(\rho E^* + p^*\right) v\right]_0 = \left[\left(\rho E^* + p^*\right) v\right]_1 \ ,$$

(6.3c)

where

$$p^* = p + \frac{1}{3}\mathbb{P}T^4 \ ,$$

(6.4a)

80

$$e^* = e + \frac{1}{\rho}\mathbb{P}T^4 \,, \tag{6.4b}$$

$$E^* = e^* + \frac{1}{2}v^2 \,. \tag{6.4c}$$

In [20], Lowrie and Rauenzahn show that these equations may be manipulated algebraically to solve for ρ_1:

$$\rho_1(T_1) = \frac{f_1(T_1) + \sqrt{f_1^2(T_1) + f_2(T_1)}}{6(\gamma - 1)T_1} \,, \tag{6.5}$$

where

$$f_1(T_1) = 3(\gamma + 1)(T_1 - 1) - \mathbb{P}\gamma(\gamma - 1)(7 + T_1^4) \,, \tag{6.6a}$$

$$f_2(T_1) = 12(\gamma - 1)^2 T_1 \left[3 + \gamma\mathbb{P}\left(1 + 7T_1^4\right)\right] \,. \tag{6.6b}$$

Furthermore, eliminating v_1 from the mass equation, substituting the result into the momentum equation, and rearranging terms, we have an equation for T_1:

$$3\rho_1(\rho_1 T_1 - 1) + \gamma\mathbb{P}\rho_1\left(T_1^4 - 1\right) = 3\gamma(\rho_1 - 1)M_0^2 \,. \tag{6.7}$$

Substituting Eq. (6.5) into Eq. (6.7), this results in a ninth-order polynomial, which may be solved numerically for T_1. We initialize this solution procedure using an estimate for T_1 based on $\mathbb{P}$. For "small" values of $\mathbb{P}$, we initialize using:

$$T_1^{est} = \frac{\left(1 - \gamma + 2\gamma M^2\right)\left(2 + (\gamma - 1)M^2\right)^2}{(\gamma + 1)^2 M^2} \,. \tag{6.8}$$

For "large" values of $\mathbb{P}$, we estimate T_1 as:

$$T_1^{est} = \sqrt[4]{\frac{8\left(\frac{M^2}{(4/9)\mathbb{P}} - 1\right)}{7}} \,. \tag{6.9}$$

81

In solving for T_1, we note that the numerical solver does not always converge to the same final value for T_1 for both initial estimates. However, for the shocks considered here, in the case when the initial estimates lead to differing values of T_1, the final solution for one estimate is always non-physical, e.g. an absorption cross-section larger than the total cross-section. So, in these cases, it is obvious which converged T_1 value is correct.

Because our radiation-hydrodynamics method is developed in dimensional form, we must also define the characteristic values $\hat{\rho}_0$ and $\hat{T}_0$. The remaining dimensional-ized values are computed from the non-dimensional parameters as follows:

$$\hat{\rho}_1 = \rho_1 r\hat{ho}_0 \,, \tag{6.10a}$$

$$\hat{T}_1 = T_1 \hat{T}_0 \,, \tag{6.10b}$$

$$\hat{a}_0 = \sqrt{\frac{\hat{\alpha}_r \hat{T}_0^{\,4}}{\hat{\rho}_0 \mathbb{P}}} \,, \tag{6.10c}$$

$$\hat{v}_0 = M\hat{a}_0 \,, \tag{6.10d}$$

$$\hat{v}_1 = v_1 \hat{a}_0 \,, \tag{6.10e}$$

$$C_v = \frac{\hat{a}_0^{\,2}}{\hat{T}_0 \gamma \, (\gamma - 1)} \,, \tag{6.10f}$$

$$\hat{\sigma}_t = \frac{c}{3\kappa \hat{a}_0} \,, \tag{6.10g}$$

$$\hat{\sigma}_a = \sigma_a \frac{\hat{a}_0}{c} \,. \tag{6.10h}$$

We initialize each radiative shock calculation by setting the left half of the spatial domain equal to the far-upstream condition and the right half equal to the downstream condition. At the boundary, we compute the fluxes using our standard Riemann solver, setting the hydrodynamic unknowns in a ghost cell just to the

other side of the boundary equal to the far-stream conditions. This adds stability to the evolution of the shock by reinforcing the steady-state solution while allowing transitional waves to exit the domain. Fig. 6.2 illustrates this concept for the right boundary. Here, we set the left unknown in an exterior ghost cell equal to the far-downstream conditions, $U_{downstream}$, and compute the boundary advection flux, $F_{N+1/2}$, using our Riemann solver.
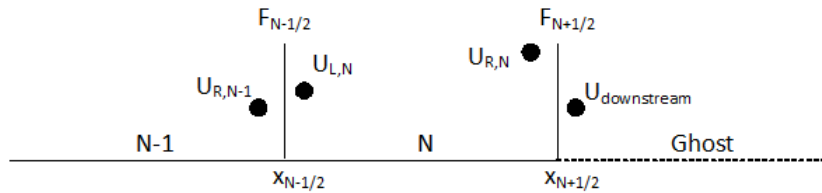

Figure 6.2: Illustration of the advection boundary conditions for the radiative shock calculations.

Because sharp slopes in LDFEMs can cause negativities in edge values, we monitor for negativities in the material temperature. If a negative temperature is detected, we set all the slopes in that cell to zero so that the edge values are equal to the cell-averages. This preserves energy conservation while eliminating non-physical temperatures at cell-edges.

To compute the time steps during the calculation, we use a similar adaptive time step control scheme to the one described in section 3.3.2.1 based on a user-specified "target temperature change", ΔT_{targ}. Again, for a given time step, the maximum

relative change is computed using:

$$\Delta T = 2 \max_i \frac{|T_i^{n+1} - T_i^n|}{T_i^{n+1} + T_i^n} . \tag{6.11}$$

However, because we use an IMEX scheme to solve our rad-hydro system, we must also limit the time step according to the Courant limit associated with the hydrodynamic advection terms. We compute this limit by determining the maximum signal velocity associated with the system and define the maximum hydrodynamic time step to be:

$$\Delta t_H = CFL \Delta x S_{max} , \tag{6.12}$$

where S_{max} is the maximum signal velocity, and CFL is the user-defined Courant condition number such that $0 \leq C \leq 1$. We use the following estimate for S_{max} outlined in [31]:

$$S_{max} = \max_{i \in [1,N]} \{ |u_i - a_i|, |u_i + a_i| \} , \tag{6.13}$$

where N is the number of cells, u_i is the velocity in cell i, and a_i is the speed of sound in cell i. We then compute the time step as follows:

$$\Delta t^{n+1} = \min \left(\frac{\Delta T_{targ}}{\Delta T} \Delta t^n, \xi \Delta t^n, \Delta t_H, t - t_{fin} \right) . \tag{6.14}$$

The second term ensures that the time step doesn't grow too rapidly by imposing a maximum allowed time step change, ξ, and the fourth term forces the final time step to end the calculation at t_{fin}. In order to ensure that the temperature doesn't vary too much, ΔT is also compared with a maximum allowed temperature change, ΔT_{max}. If $\Delta T > \Delta T_{max}$, then the time step $\Delta t^{n+1/2}$ is reduced by a factor of 1/3,

and the calculation is repeated from t_n. In our calculations, we set $CFL = 0.3$, $\Delta T_{targ} = 1.01$, $\Delta T_{max} = 1.012$, and $\xi = 1.5$.

6.3 Radiative Shock Solutions

We test our algorithm over a range of the radiative shocks presented in [17]. These shocks incorporate a variety of the features described in Section 6.1. For each of these shocks, we set $\mathbb{P} = 1e-4$, $\gamma = 5/3$, $\kappa = 1$, and $\sigma_a = 1e6$, and the material properties are given in Table 6.1.

First, we compute the Mach 1.2 shock, which has a hydrodynamic shock but no ISP. Table 6.2 shows the initial conditions; the final time of the calculation is 0.5 shakes. Figs. 6.3 and 6.4 compare our results with the semi-analytic solutions for the density and fluid and radiation temperatures, respectively, and again, we see good agreement between the two. In this solution, we see a discontinuity in both the density and material temperature due to the hydrodynamic shock, and the maximum temperature is bounded by the far-downstream temperature, since there is no ISP to drive it further.

Table 6.1: Material properties for radiative shock calculations.

$\hat{\sigma}_a$	3.9071164263502112e+002
$\hat{\sigma}_t$	8.5314410158161809e+002
$\hat{C}_v$	1.2348000000000001e-001

Table 6.2: Mach 1.2 initial conditions.

|	Pre-shock	Post-shock
$\hat{\rho}$	1.0000000000000000e+00	1.2973213452231311e+000
$\hat{u}$	1.4055888445772469e-001	1.0834546504247138e-001
$\hat{T}$	1.0000000000000001e-001	1.1947515210501813e-001
$\hat{\rho}\hat{u}$	1.4055888445772469e-001	1.4055888445772469e-001
$\hat{E}$	2.2226400000000000e-002	2.6753570531538713e-002
$\hat{E}_r$	1.3720000000000002e-006	2.7955320762182542e-006
$4/3\hat{E}\hat{u}$	2.5712905263466435e-007	4.0384429711868299e-007
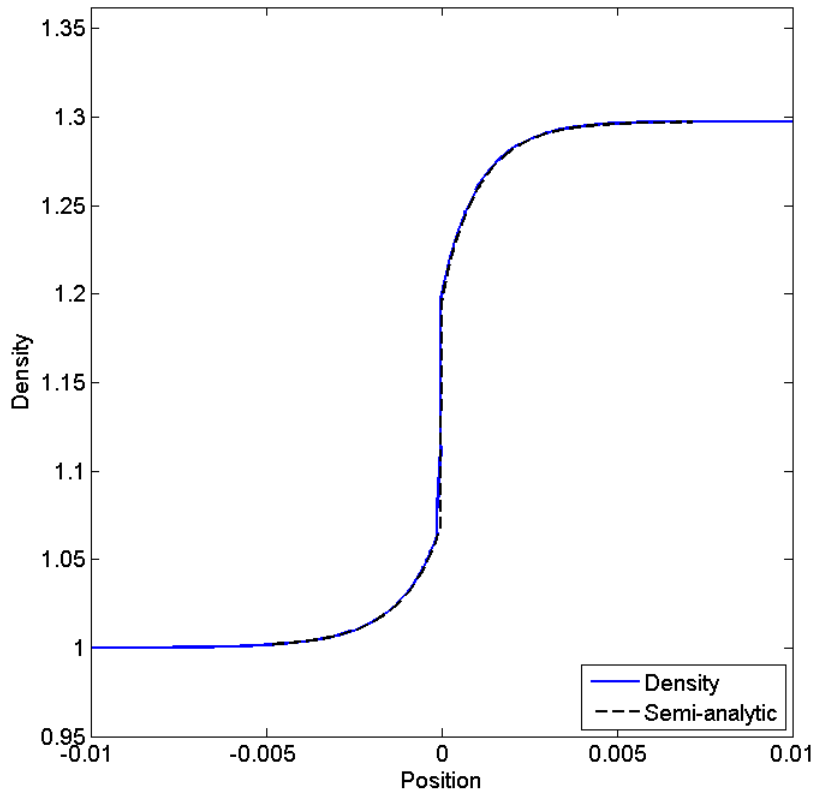
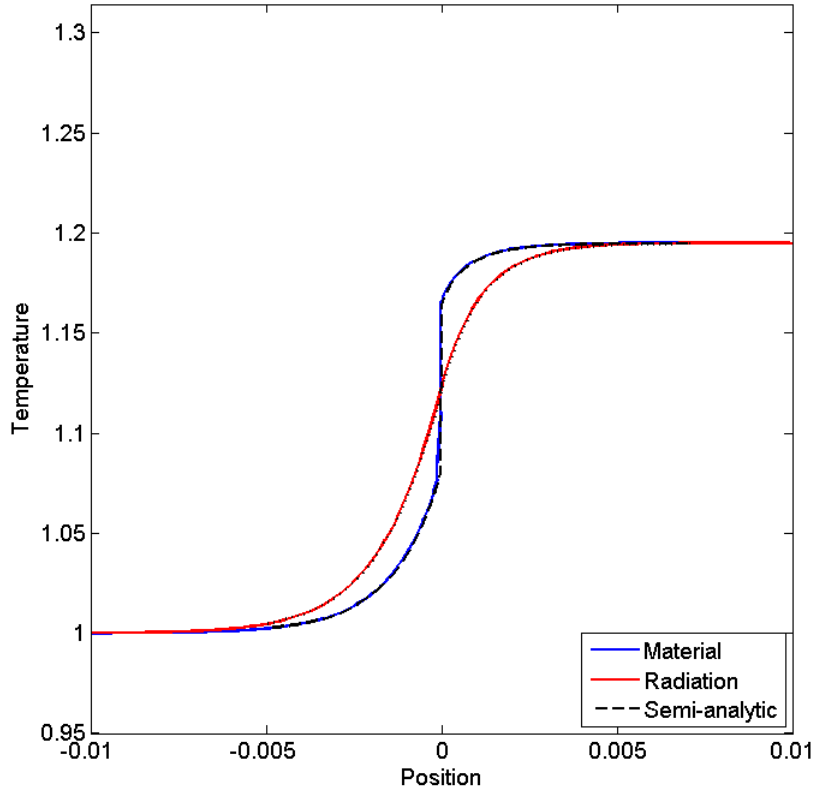Figure 6.3: Mach 1.2 radiative shock density.

Figure 6.4: Mach 1.2 radiative shock material and radiation temperatures.

The most structurally complex shock that we compute is the Mach 2 shock, which has both a hydrodynamic shock and an ISP. The initial conditions are given by Table 6.3, and the final time of the calculation is 1 shake. Figs. 6.5 and 6.6 show our results compared with the semi-analytic solutions. In each of these figures, we can see the effects of the hydrodynamic shock, causing a discontinuity in both the material density and temperature. We can also see the Zel'dovich spike, caused by the ISP embedded within the hydrodynamic shock, driving up the material temperature at the shock front. This spike leads to the relaxation region downstream as the material temperature and radiation temperature equilibrate. Fig. 6.7 shows the

Table 6.3: Mach 2 initial conditions.

	Pre-shock	Post-shock
$\hat{\rho}$	1.0000000000000000e+00	2.2860748989303659e+000
$\hat{u}$	2.3426480742954117e-001	1.0247468599526272e-001
$\hat{T}$	1.0000000000000001e-001	2.0775699953301918e-001
$\hat{\rho}\hat{u}$	2.3426480742954117e-001	2.3426480742954117e-001
$\hat{E}$	3.9788000000000004e-002	7.0649692950433357e-002
$\hat{E}_r$	1.3720000000000002e-006	2.5560936967521927e-005
$4/3\hat{E}\hat{u}$	4.285842105777400e-007	3.4924653193220162e-006

Zel'dovich spike and relaxation region in more detail. Here, we can see that our results still show very good agreement with the semi-analytic solution.
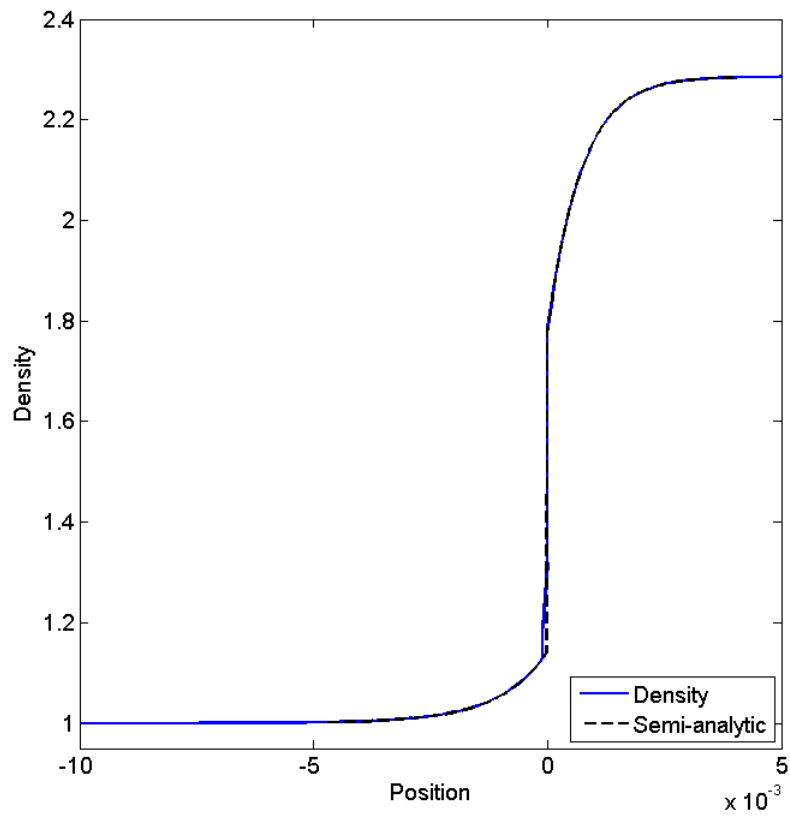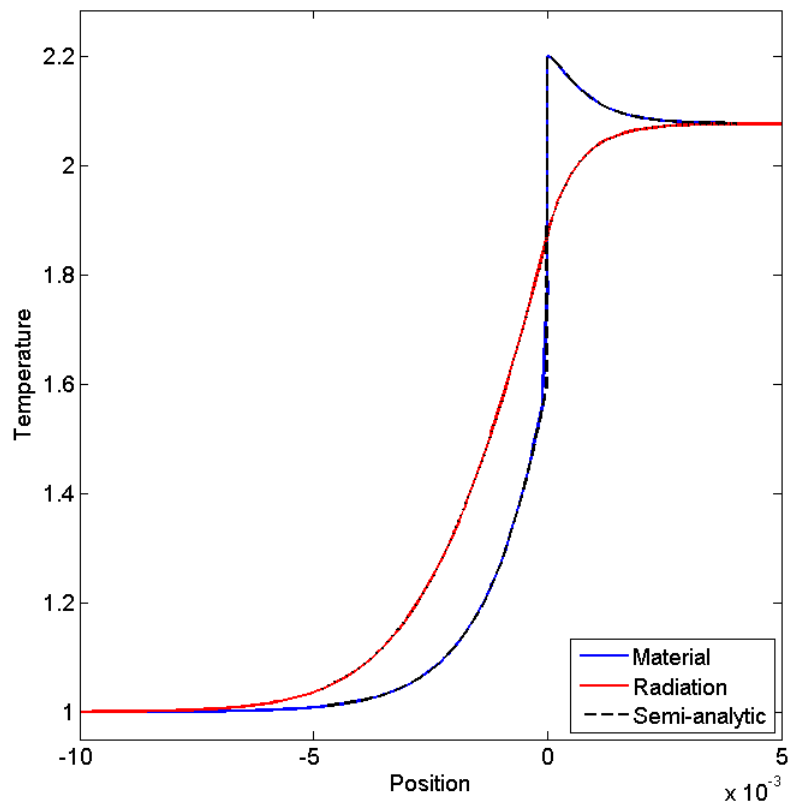
Figure 6.5: Mach 2 radiative shock density.

Figure 6.6: Mach 2 radiative shock material and radiation temperatures.
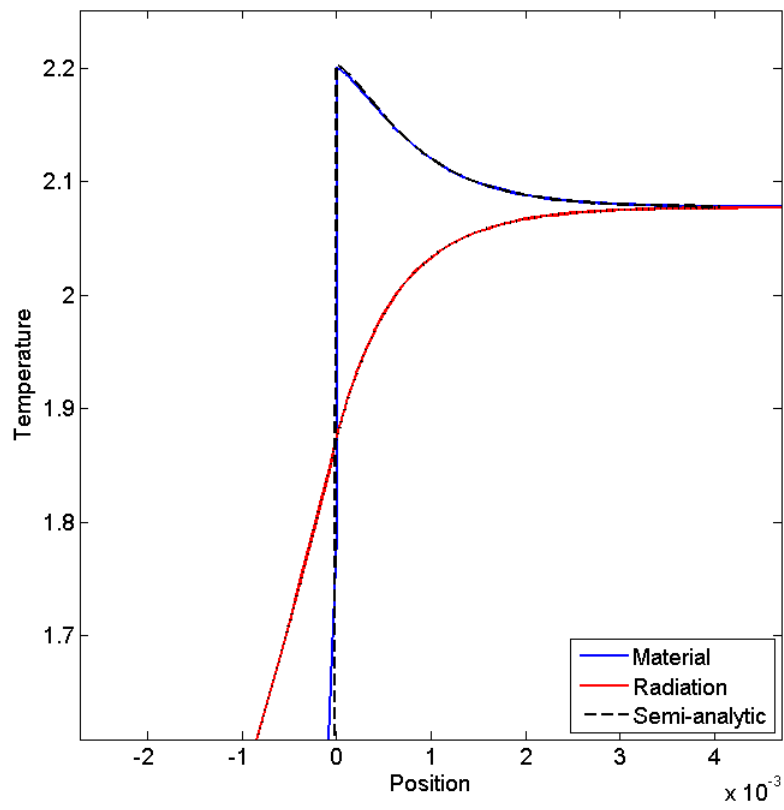
Figure 6.7: Zel'dovich spike and relaxation region of Mach 2 shock.

Finally, we reproduce the Mach 50 radiative shock solution. This shock has no hydrodynamic discontinuity or ISP; however, it is the most computationally intensive to compute. This is due to the fact that the large discontinuity in the initial conditions causes sharp slopes leading to negativities in the edge values of the material temperature in the beginning steps of the calculation. Furthermore, large, rapid temperature variations force time-step restarts described in Section 6.2, and high fluid wave speeds restrict the time step size throughout the calculation. The initial conditions for this shock are provided in Table 6.4, and the final time of the calculation is 1.5 shakes. The results of this calculation are compared with semi-analytic solutions in Figs. 6.8 and 6.9. Note that the structure of the precursor for the Mach 50 shock differs from that of the Mach 1.2 and Mach 2 shocks in that the diffusive precursor is much more dominant in the Mach 50 shock; whereas, the others have a much larger transmissive precursor. As with the other shocks, we continue to see good overall agreement between our results and the semi-analytic solutions.

Table 6.4: Mach 50 initial conditions.

|	Pre-shock	Post-shock
$\hat{\rho}$	1.0000000000000000e+00	6.5189217901173153e+000
$\hat{u}$	5.8566201857385289e+000	8.9840319830453630e-001
$\hat{T}$	1.0000000000000001e-001	8.5515528368625038e+000
$\hat{\rho}\hat{u}$	5.8566201857385289e+000	5.8566201857385289e+000
$\hat{E}$	1.7162348000000001e+001	9.5144308747326214e+000
$\hat{E}_r$	1.3720000000000002e-006	7.3372623010289956e+001
$4/3\hat{E}\hat{u}$	1.0713710526444349e-005	8.7890932240583339e+001
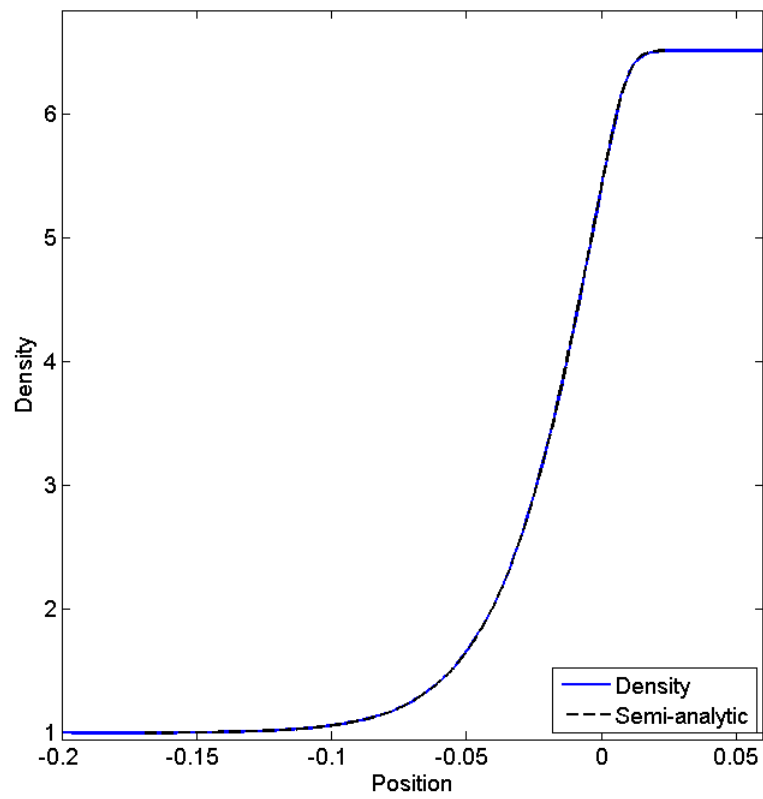
Figure 6.8: Mach 50 radiative shock density.
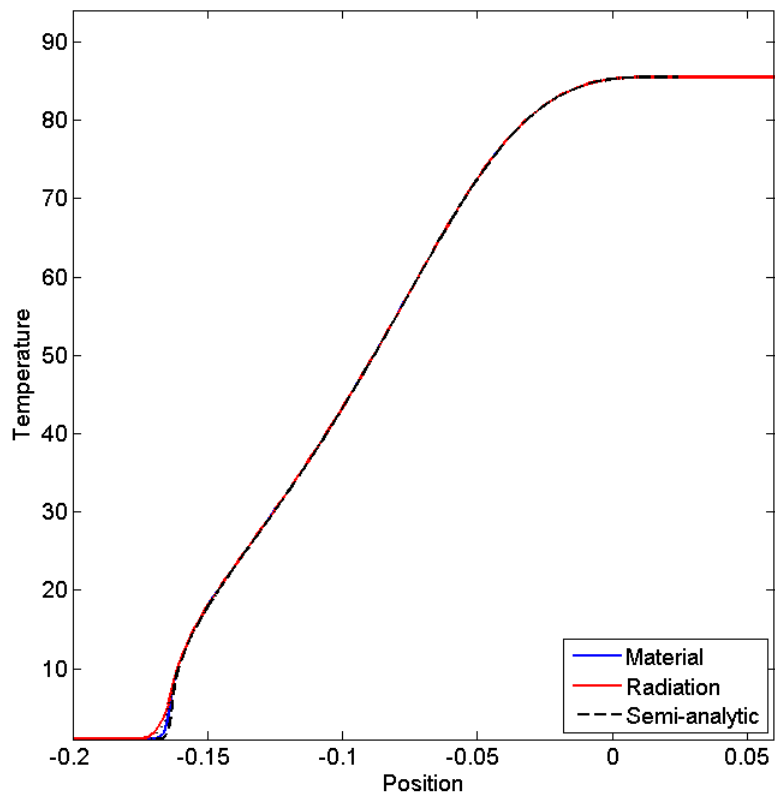
Figure 6.9: Mach 50 radiative shock material and radiation temperatures.

6.4   Comparison of Our Second-Order Method with a First-Order Scheme

To demonstrate the effectiveness of our second-order method in solving radiative shock problems, we use the Mach 50 radiative shock solution and compare results from our method with those from a first-order scheme; though, we note that both methods will be first-order for problems with a discontinuity. This scheme consists of a full MUSCL-Hancock step to compute the fluid advection component, followed by an explicit update to the momentum to account for radiation momentum deposition, and a Crank-Nicholson radiative transfer calculation over the full time-step to compute the radiation quantities and to update the internal energy. Thus, our first-order method is actually a first-order coupling of some of the second-order components used in our full second-order scheme. We begin the first-order method with the standard MHM data reconstruction and evolution steps:

$$U_{L,i}^n = U_i^n - \frac{\Delta_i^n}{2}; \quad U_{R,i}^n = U_i^n + \frac{\Delta_i^n}{2}, \tag{6.15}$$

$$U_i^{n+1/2} = U_i^n + \frac{\Delta t}{2\Delta x} \left(F_{L,i}^n - F_{R,i}^n \right) . \tag{6.16}$$

Next, as with our second-order calculation, we reconstruct the half-step unknowns and use the Riemann solver to compute the cell edge fluxes $F_{i+1/2}^{n+1/2}$. Then, we complete the MHM advection step with a Godunov calculation:

$$U_i^* = U_i^n + \frac{\Delta t}{\Delta x} \left(F_{i-1/2}^{n+1/2} - F_{i+1/2}^{n+1/2} \right) . \tag{6.17}$$

Once this is computed, we update the fluid momentum explicitly using the cell-averaged radiation momentum deposition:

$$\frac{\rho_i^{n+1}\left(u_i^{n+1} - u_i^*\right)}{\Delta t} = \frac{1}{2}\frac{\sigma_{t,L,i}^n}{c}\left(F_{r,L,i}^n - \frac{4}{3}E_{r,L,i}^n u_{L,i}^n\right)$$
$$+\frac{1}{2}\frac{\sigma_{t,R,i}^n}{c}\left(F_{r,R,i}^n - \frac{4}{3}E_{r,R,i}^n u_{R,i}^n\right) . \qquad (6.18)$$

Then, we solve the radiative transfer equations using the Crank-Nicholson method to compute the radiation energy density and radiation current and to update the material energy:

$$\frac{\left(E_r^{n+1,k+1} - E_r^n\right)}{\Delta t} = -\frac{1}{2}\left(\frac{\partial F^{n+1,k+1}}{\partial x} + \frac{\partial F^n}{\partial x}\right) + \frac{\sigma_a^n c}{2}\left(a(T^n)^4 - E_r^n\right)$$
$$+\frac{\sigma_a^{n+1,k}c}{2}\left(a(T^{n+1,k+1})^4 - E_r^{n+1,k+1}\right)$$
$$+\sigma_t^n\frac{u^n}{c}\left(\frac{4}{3}E_r^n u^n - F_r^n\right) , \qquad (6.19a)$$

$$\frac{1}{3}\frac{\partial E_r^{n+1,k+1}}{\partial x} + \frac{1}{3}\frac{\partial E_r^n}{\partial x} + \frac{\sigma_t^{n+1,k}}{c}F^{n+1,k+1} + \frac{\sigma_t^n}{c}F^n =$$
$$\sigma_t^{n+1,k}\frac{4}{3}E^{n+1,k+1}\frac{u^{n+1}}{c} + \sigma_t^n\frac{4}{3}E^n\frac{u^n}{c} , \qquad (6.19b)$$

$$\frac{\left(E^{n+1,k+1} - E^*\right)}{\Delta t} = -\frac{\sigma_a^{n+1,k}c}{2}\left(a(T^{n+1,k+1})^4 - E_r^{n+1,k+1}\right)$$
$$-\frac{\sigma_a^n c}{2}\left(a(T^n)^4 - E_r^n\right)$$
$$-\sigma_t^n\frac{u^n}{c}\left(\frac{4}{3}E_r^n u^n - F_r^n\right) . \qquad (6.19c)$$

In order to compare these methods to a solution that varies in both space and time, we uniformly increase the velocity of the semi-analytic Mach 50 shock solution

96

Table 6.5: Comparison of the computational work required to compute the solution of the Mach 50 shock for the first and second-order methods.

	Number of Time Steps	Avg. Non-linear Iters. per Step	Total Advection Solves	Total Diffusion Solves
First-Order	382	27.78	382	9085
Second-Order	158	19.07	316	3013

by some speed, S_{shock}. Due to the Galilean invariance of the shock solution, the shock profile remains unchanged; however, now, it propagates through the fluid at S_{shock}, making the solution time-dependent. For this test, we initialize our calculations with the original, semi-analytic shock profile and compute the solution for a shock moving at $S_{shock} = 1$ cm/shake for 0.04 shakes using 40 cells. As with our other shock calculations, we use adaptive time step controls setting $CFL = 0.3$, $\Delta T_{targ} = 1.01$, $\Delta T_{max} = 1.012$, and $\xi = 1.5$.

Figs. 6.10, 6.11, and 6.12 show the comparison of the first and second-order methods to the semi-analytic solution for the density, material temperature, and radiation temperature, respectively, and Table 6.5 shows the work required to obtain these results. From these results, we see that, for this problem, our second-order scheme is consistently more accurate than the first-order scheme and requires 20% fewer advection solves and 1/3 as many diffusion solves to compute the solution using the same time step control criteria.
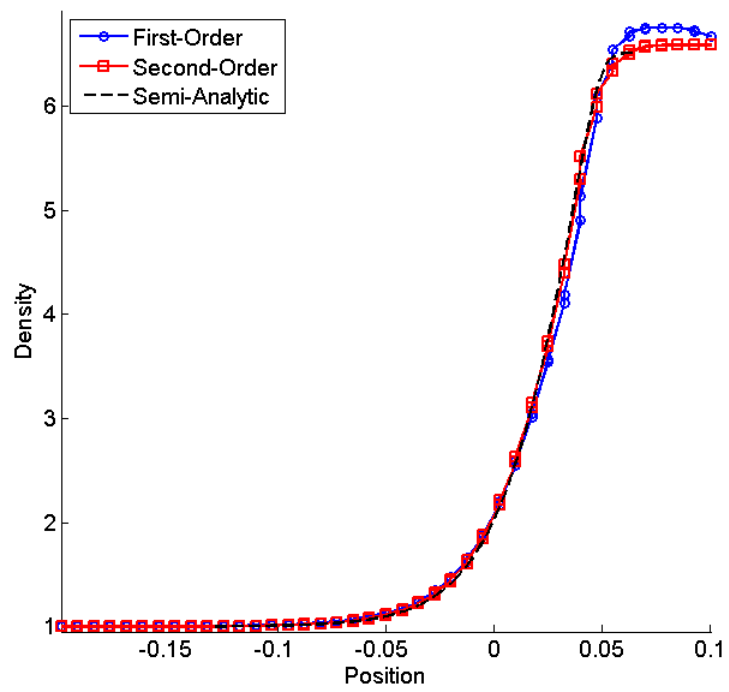
Figure 6.10: Comparison of first- and second-order method results for the density of the Mach 50 radiative shock problem.
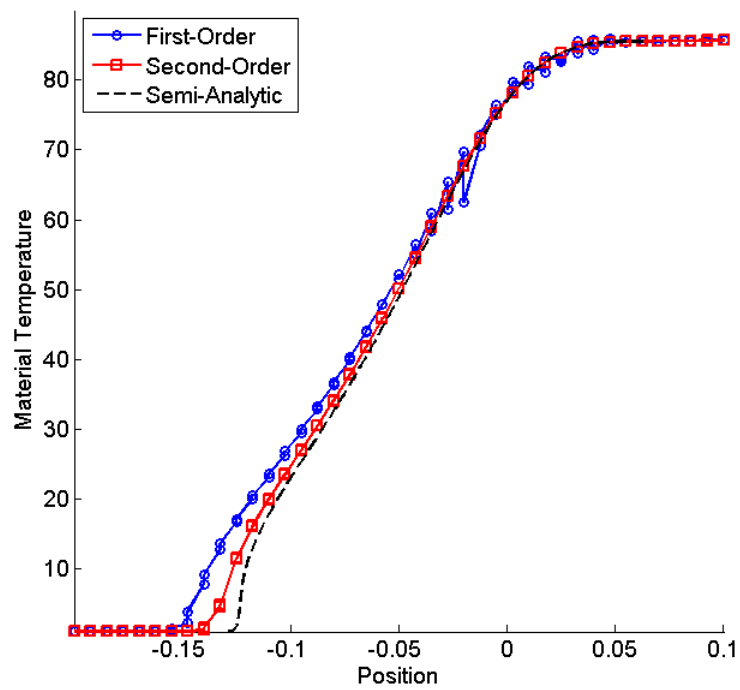
Figure 6.11: Comparison of first- and second-order method results for the material temperature of the Mach 50 radiative shock problem.
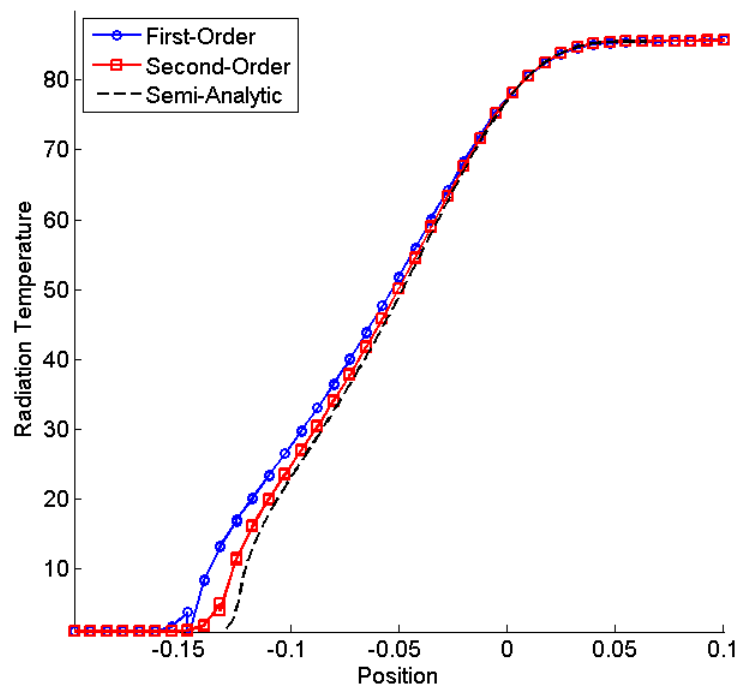
Figure 6.12: Comparison of first- and second-order method results for the radiation temperature of the Mach 50 radiative shock problem.

7. SUMMARY

Our scheme combines the MUSCL-Hancock Method for solving 1-D fluid advection problems with a grey radiation diffusion model discretized using a linearly-discontinuous finite element method in space and the TR/BDF2 scheme in time. MUSCL-Hancock is a second-order, explicit method widely used to solve fluid advection problems. The LDFEM is a popular spatial discretization for radiation transport, since it is second-order accurate, preserves the diffusion limit, and permits discontinuities at cell-edges. While this scheme is not frequently used for radiation diffusion, we choose it in anticipation of the extension of our scheme to a radiation transport model and to show how the challenges of blending these spatial discretizations may be overcome. The radiation-hydrodynamics scheme, itself, consists of two predictor-corrector cycles. Each cycle includes the full MUSCL-Hancock method to compute the fluid advection over half of the time step. The first cycle uses Crank-Nicholson, i.e. the trapezoid rule, to compute the radiation diffusion and energy exchange over the first half time step, and the second cycle uses this result with the BDF2 scheme to compute the solution over the remainder of the step, yielding the full TR/BDF2 solution. For problems in which the time step is determined by the time scale of the fluid, this design amortizes the cost of the non-linear, implicit radiation solves over effectively two hydrodynamic time steps.

While the TR/BDF2 scheme is not well-known in the radiation transport community, we show in Section 3 how it may be applied to the equations of radiative transfer. Using the TR/BDF2 method, we, also, test a variety of approaches for treating the non-linear terms in the radiative transfer equations stemming from the blackbody emission source and the temperature dependent cross-sections. We

compare fully-converged and fixed-iteration versions of Newton and hybrid Newton-Picard methods for both accuracy and efficiency. Here, we find that the converged schemes are consistently the most accurate; whereas, the single-iteration Newton method is the most efficient for our test problems. We, also, find that, in some cases, the converged hybrid scheme is actually more efficient than the fixed-iteration version. Given these results, we use the converged hybrid Newton-Picard scheme for our radiation-hydrodynamics algorithm, due to its high level of accuracy, its easy application to both continuous and tabular cross-section data, and its adherence to the maximum principle. Furthermore, as shown in Section 2, the TR/BDF2 scheme damps oscillations much more effectively than Crank-Nicholson.

We demonstrate how the discrepancies in slope definitions between the radiation and hydrodynamics schemes may be overcome to preserve both second-order accuracy and the diffusion limit. While possibly not immediately apparent, this is an important property. As discussed in Section 1, verifying that a radiation transport spatial discretization has the diffusion limit is crucial for ensuring the accuracy of solutions in which computational limits require a spatial cell to encompass many mean-free paths. This is often the case for radiation transport calculations in highly-scattering media or in radiative transfer calculations in which absorption and re-emission dominate the transport process, e.g. the radiative shocks discussed in Section 6. By preserving the LD slopes between implicit solves, the extension of our method to a similarly discretized radiation transport model is straightforward. We believe this approach also preserves the diffusion limit in such a way that the radiation solution will preserve the diffusion limit in 2D and 3D despite the use of hydrodynamic limiters for the fluid unknowns that otherwise would not.

Using the Method of Manufactured Solutions, we demonstrate in Section 5 that our algorithm is second-order accurate in the equilibrium diffusion limit and the

102

streaming limit. To accomplish this, we derive forcing functions that, when used as source terms in our radiation-hydrodynamics system, yield a prescribed set of exact solutions. We compare these exact solutions with our computational results to observe the behavior of the true model error. In both the streaming and equilibrium diffusion limits, our method consistently shows second-order accuracy in space and time for both the radiation and hydrodynamic unknowns.

In order for a radiation-hydrodynamics algorithm to be useful in practical applications, it is necessary for the algorithm to be able to accurately compute radiative shocks. In Section 6, we test our method using a set of representative shock problems and compare our results with semi-analytic solutions. The Mach 1.2 and Mach 2 radiative shock problems represent structurally complex shocks, having a hydrodynamic shock, which produces a discontinuity in the hydrodynamic unknowns, and in the case of the Mach 2 shock, an ISP, which produces a Zel'dovich spike. Our method reproduces these shocks very well, even in the region of the Zel'dovich spike. The Mach 50 radiative shock problem represents a very computationally challenging shock. While the final shock solution, itself, is continuous, the large initial discontinuity leads to very sharp slopes in the first few time steps potentially leading to negativities in the temperature, and the rapid variation of the solution forces many time step readjustments. In our results, again, we see that our method reproduces this shock well.

8.   CONCLUSIONS AND FUTURE WORK

We develop a new IMEX method for solving the 1-D equations of radiation-hydrodynamics that is second-order accurate in space and time. In addition to accuracy, we meet the goals outlined in Section 1: it reliably converges non-linearities, rapidly damps oscillations, incorporates modern algorithms used by the hydrodynamics and radiation transport communities, appears to have straightforward extensibility to a full radiation transport model, preserves the diffusion limit in 1D in such a way that it is expected to preserve this limit in 2D and 3D, accurately computes radiative shocks, and reduces to fundamental algorithms when the effects of coupled physics are negligible. Thus, it represents a very useful alternative to existing methods.

In future work, we recommend extending our radiation solver to incorporate a radiation transport model. The structure of our radiation-hydrodynamics algorithm should make this extension straightforward. Since our algorithm only requires the angle-integrated radiation energy density and radiation current, the radiation solver may, in some sense, be treated as a black box module to compute these quantities. Of course, the angular intensities will need to be preserved across time steps. The only significant change required for this extension would be to make the momentum updates implicit to conserve momentum as well as energy.

REFERENCES

[1] T. S. Axelrod, P. F. Dubois, and C. E. Rhoades Jr. An Implicit Scheme for Calculating Time- and Frequency-Dependent Flux Limited Radiation Diffusion in One Dimension. *Journal of Computational Physics*, 54:205–220, 1984.

[2] R. E. Bank, W. M. Coughran, Jr., W. Fichtner, E. H. Grosse, D. J. Rose, and R. K. Smith. Transient Simulation of Silicon Devices and Circuits. *IEEE Transactions on Computer-Aided Design of Integrated Circuits and Systems*, 4:436–451, 1985.

[3] J. W. Bates, D. A. Knoll, W. J. Rider, R. B. Lowrie, and V. A. Mousseau. On Consistent Time-Integration Methods for Radiation Hydrodynamics in the Equilibrium Diffusion Limit: Low-Energy-Density Regime. *Journal of Computational Physics*, 167:99–130, 2001.

[4] P. N. Brown, D. E. Shumaker, and C. S. Woodward. Fully Implicit Solution of Large-Scale Non-equilibrium Radiation Diffusion with High Order Time Integration. *Journal of Computational Physics*, 204:760–783, 2005.

[5] W. Dai and P. R. Woodward. Numerical Simulations for Radiation Hydrodynamics. I. Diffusion Limit. *Journal of Computational Physics*, 142:182–207, 1998.

[6] R. P. Drake. Theory of Radiative Shocks in Optically Thick Media. *Physics of Plasmas*, 14:043301:1–10, 2007.

[7] J. D. Edwards and J. E. Morel. Nonlinear Variants of the TR/BDF2 Method for Thermal Radiative Diffusion. *Journal of Computational Physics*, 230:1198–1214, 2011.

[8] E. Hairer and G. Wanner. *Solving Ordinary Differential Equations II.* Springer, 2002.

[9] S. Y. Kadioglu. A Fully Second Order Implicit/Explicit Time Integration Technique for Hydrodynamics Plus Nonlinear Heat Conduction Problems. *Journal of Computational Physics*, 9:3237–3249, 2010.

[10] S. Y. Kadioglu. A Second Order Self-Consistent IMEX Method for Radiation Hydrodynamics. *Journal of Computational Physics*, 229:8313–8332, 2010.

[11] D. A. Knoll, R. B. Lowrie, and J. E. Morel. Numerical Analysis of Time-Integration Errors for Non-equilibrium Radiation Diffusion. *Journal of Computational Physics*, 226:1332–1347, 2007.

[12] A. Kurganov, G. Petrova, and B. Popov. Adaptive Semi-Discrete Central-Upwind Schemes. *SIAM Journal of Scientific Computing*, 29:2381–2401, 2007.

[13] E. W. Larsen and B. Mercier. Analysis of a Monte Carlo Method for Nonlinear Radiative Transfer. *Journal of Computational Physics*, 71:50–64, 1987.

[14] E. W. Larsen, J. E. Morel, and Jr. W. F. Miller. Asymptotic Solutions of Numerical Transport Problems in Optically Thick, Diffusive Regimes. *Journal of Computational Physics*, 69:283–324, 1987.

[15] P. D. Lax. *Hyperbolic Systems of Conservation Laws and the Mathematical Theory of Shock Waves.* CBMS Regional Conf. Ser. In Appl. Math. 11, 1972.

[16] R. B. Lowrie. A Comparison of Implicit Time Integration Methods for Nonlinear Relaxation and Diffusion. *Journal of Computational Physics*, 196:566–590, 2004.

[17] R. B. Lowrie and J. D. Edwards. Radiative Shock Solutions with Grey Non-equilibrium Diffusion. *Shock Waves*, 18:129–143, 2008.

[18] R. B. Lowrie and J. E. Morel. Issues with High-Resolution Godunov Methods for Radiation Hydrodynamics. *Journal of Quantitative Spectroscopy & Radiative Transfer*, 69:475–489, 2001.

[19] R. B. Lowrie, J. E. Morel, and J. A. Hittinger. The Coupling of Radiation and Hydrodynamics. *Astrophysics Journal*, 521:432–450, 1999.

[20] R.B. Lowrie and R.M. Rauenzahn. Radiative Shock Solutions in the Equilibrium-Diffusion Limit. *Shock Waves*, 16:445–453, 2007.

[21] R. G. McClarren, T. M. Evans, R. B. Lowrie, and J. D. Densmore. Semi-Implicit Time Integration for Pn Thermal Radiative Transfer. *Journal of Computational Physics*, 196:566–590, 2004.

[22] R. G. McClarren and R. B. Lowrie. Manufactured Solutions for the P1 Radiation-Hydrodynamics Equations. *Journal of Quantitative Spectroscopy & Radiative Transfer*, 109:2590–2602, 2008.

[23] D. Mihalas and B. Weibel-Mihalas. *Foundations of Radiation Hydrodynamics*. Dover Publications, Inc, 1999.

[24] J. E. Morel. Discrete Ordinates Methods for Radiative Transfer in the Non-Relativistic Stellar Regime. *Computational Methods in Transport: Lecture Notes in Computational Science and Engineering*, 48:69–81, Springer, 2006.

[25] G. L. Olson. Second-Order Time Evolution of Pn Equations for Radiation Transport. *Journal of Computational Physics*, 228:3027–3083, 2009.

[26] W. H. Reed and T. R. Hill. Triangular Mesh Methods for the Neutron Transport Equation. Technical report, Los Alamos Scientific Laboratory, 1973.

[27] A.B. Reighard. Observation of Collapsing Radiative Shocks in Laboratory Experiments. *Physics of Plasmas*, 13, 2006.

[28] M. Sekora and J. Stone. A Higher Order Godunov Method for Radiation Hydrodynamics: Radiation Subsystem. *Communication in Applied and Computational Mathematics*, 4:135–152, 2009.

[29] J. Stoer and J. Bulirsch. *Introduction to Numerical Analysis*. Springer, 2002.

[30] J. M. Stone and D. Mihalas. Upwind Monotonic Interpolation Methods for the Solution of the Time Dependent Radiative Transfer Equation. *Journal of Computational Physics*, 100:402–408, 1992.

[31] E.F. Toro. *Riemann Solvers and Numerical Methods for Fluid Dynamics: A Practical Introduction*. Springer, 1999.

[32] T. A. Wareing, J. E. Morel, and J. M. McGhee. A Diffusion Synthetic Acceleration Method for the Sn Equations with Discontinuous Finite Element Space and Time Differencing. In *Proceedings of the International Conference on Mathematics and Computation, Reactor Physics and Environmental Analyses in Nuclear Applications*, 1999.

[33] J. S. Warsa, T. A. Wareing, and J. E. Morel. Fully Consistent Diffusion Synthetic Acceleration of Linear Discontinuous Transport Discretizations on Three-

Dimensional Unstructured Meshes. *Nuclear Science and Engineering*, 141:236–251, 2002.

[34] J. S. Warsa, T. A. Wareing, and J. E. Morel. Solution of the Discontinuous P1 Equations in Two-Dimensional Cartesian Geometry with Two-Level Preconditioning. *SIAM Journal of Scientific Computing*, 24:2093–2124, 2003.

[35] Ya. B. Zel'dovich and Yu. P. Raizer. *Physics of Shock Waves and High-Temperature Hydrodynamic Phenomena*. Dover Publications, Inc, 2002.